Monthly Notices of the ROYAL ASTRONOMICAL SOCIETY

MNRAS **547,** 1–22 (2026) https://doi.org/10.1093/mnras/stag070
Advance Access publication 2026 January 13

Two temperate Earth- and Neptune-sized planets orbiting fully convective M dwarfs

Madison G. Scott [1★†] Georgina Dransfield [2,3,1★†] Mathilde Timmermans [1,4] Amaury H.M.J. Triaud [1] Benjamin V. Rackham [5,6] Khalid Barkaoui [7,4,5] Adam J. Burgasser [8] Karen A. Collins [9] Michaël Gillon [4] Steve B. Howell [10] Alan M. Levine,[6] Francisco J. Pozuelos [11] Keivan G. Stassun [12] Carl Ziegler [13] Yilen Gomez Maqueo Chew [14] Catherine A. Clark [15] Yasmin Davis [1] Fatemeh Davoudi [4] Tansu Daylan [16] Brice-Olivier Demory [17] Dax Feliz [18] Akihiko Fukui [19,7] Maximilian N. Günther [20] Emmanuël Jehin,[21] Florian Lienhard [22] Andrew W. Mann [23] Clàudia Janó Muñoz [24] Norio Narita [19,25,7] Peter P. Pedersen,[24,22] Richard P. Schwarz [9] Avi Shporer [6] Abderahmane Soubkiou [4] and Sebastián Zúñiga-Fernández [4]

Affiliations are listed at the end of the paper

Accepted 2025 December 19. Received 2025 December 9; in original form 2025 October 31

ABSTRACT

As the diversity of exoplanets continues to grow, it is important to revisit assumptions about habitability and classical habitable zone definitions. In this work, we introduce an expanded 'temperate' zone, defined by instellation fluxes in the range $0.1 < S/S_\oplus < 5$, thus encompassing a broader range of potentially habitable worlds. We also introduce the TEMPOS survey, which aims to produce a catalogue of precise radii for temperate planets orbiting M dwarfs with $T_{\rm eff} \leq 3400$ K. This work reports the discovery and characterization of two planets in this temperate regime orbiting mid-type M dwarfs: TOI-6716 b, a $R_b = 0.98 \pm 0.07\,R_\oplus$ planet orbiting its M4 host star ($R_\star = 0.231 \pm 0.015 R_\odot$, $M_\star = 0.223 \pm 0.011\,M_\odot$, $T_{\rm eff} = 3110 \pm 80$ K) with a period $P = 4.7185898^{+0.0000054}_{-0.0000041}$ d, and TOI-7384 b, a $R_b = 3.56 \pm 0.21\,R_\oplus$ planet orbiting an M4 ($R_\star = 0.319 \pm 0.018 R_\odot$, $M_\star = 0.318 \pm 0.016\,M_\odot$, $T_{\rm eff} = 3185 \pm 75$ K) star every $P = 6.2340258^{+0.0000034}_{-0.0000036}$ d. The radii of TOI-6716 b and TOI-7384 b have precisions of 6.8 per cent and 5.9 per cent, respectively. We validate these planets with multiband ground-based photometric observations, high-resolution imaging, and statistical analyses. We find these planets to have instellation fluxes close to the inner (hotter) edge of the temperate zone, with $S_b = 4.4 \pm 1.1\,S_\oplus$ and $S_b = 4.9 \pm 1.1\,S_\oplus$ for TOI-6716 b and TOI-7384 b, respectively. Also, with a predicted transmission spectroscopy metric similar to the TRAPPIST-1 planets, TOI-6716 b is likely to be a good rocky-world *James Webb Space Telescope* target, should it have retained its atmosphere.

Key words: planets and satellites: detection – planets and satellites: fundamental parameters – planets and satellites: gaseous planets – planets and satellites: terrestrial planets – stars: low-mass.

1 INTRODUCTION

The search for transiting temperate planets, where for the purpose of this paper we define 'temperate' as a planet with instellation flux $0.1 \leq S/S_\oplus \leq 5$, around solar-like stars is notoriously challenging. This is because planet equilibrium temperature scales with both semimajor axis and stellar effective temperature, leading to low transit probabilities. However, due to the lower effective temperatures of M-type stars, and in particular mid- to late-type M dwarfs (≤ 3400 K), temperate planets orbiting such stars are far more likely to transit, and therefore become more accessible in transit surveys (e.g. L. Delrez et al. 2022; G. Dransfield et al. 2023; S. Dholakia et al. 2024). Additionally, due to the relatively small sizes of the M dwarf host stars, Earth-sized temperate planets produce deeper and more detectable transit signals than a similar planet orbiting a solar-type star (e.g. depths ~ 0.3–13 ppt for the M dwarf radius range $0.08 \leq R_\star/R_\odot \leq 0.5$, compared with ~ 0.1 ppt for a $R_\star = 1 R_\odot$ star). This allows for more precise constraints on parameters such as planetary radius, inclination, and orbital period from photometric data using both

★ E-mail: mgs947@student.bham.ac.uk (MGS); george.dransfield@magd.ox.ac.uk (GD)
† These two authors contributed equally to this work and should be considered joint first authors.

space-based (e.g. *TESS*; G. R. Ricker et al. 2015) and ground-based telescopes (e.g. SPECULOOS; D. Sebastian et al. 2021). A further benefit is that the measurement of precise planetary masses of smaller planets via radial velocities may be facilitated by the higher planet-to-star mass ratios (see e.g. J. A. Dittmann et al. 2017; D. A. Turner et al. 2025).

To date, 281 temperate planets have been confirmed (90 transiting.[1]), with just less than half (118) orbiting M dwarfs ($\leq$ 4000 K). Of these, 39 have been identified by *TESS* (see e.g. C. Cadieux et al. 2022; F. Murgas et al. 2023; M. Timmermans et al. 2024). Temperate planets account for only 2.6 per cent of all confirmed planets to date; this is unsurprising given most known systems are hosted by FGK stars and transit survey missions to date have had limited sensitivity to long orbital periods. For example, typical *TESS* observations of targets outside the continuous viewing zone span only ∼27 d every 2 yr; we calculate that for a temperate planet around an FGK-type star, the expected orbital periods would be in the range of ∼21 d (∼K9V, $T_{\rm eff} \simeq 3930$ K) to ∼7200 d (∼F0V, $T_{\rm eff} \simeq 7220$ K). Even the shortest of these periods often result in, at most, a single observed transit per sector, making them difficult to identify as a planet candidate. In contrast, for mid- to late-type M dwarfs, the corresponding period range shifts from 0.9 d (∼M9V, $T_{\rm eff} \simeq 2380$ K) to 147 d (∼M3V, $T_{\rm eff} = 3400$ K), bringing a much larger fraction of the temperate planet population within the detectability window of *TESS* and other transit surveys. Consequently, late-type M dwarfs represent a favourable stellar population for identifying temperate-zone planets. A key example of this is the temperate TRAPPIST-1 planets, whose orbital periods lie in the range 1.5–18.8 d with instellation fluxes in the range $0.13 \lesssim S/S_\oplus \lesssim 4.3$ (M. Gillon et al. 2017).

A 'temperate zone' has not formally been defined in the literature, but its value lies in broadening current ideas of Earth-centric habitability. This approach expands the classical HZ described by J. F. Kasting, D. P. Whitmire & R. T. Reynolds (1993) and R. K. Kopparapu et al. (2014). Planets that may fall outside this traditional metric, such as Hycean or water worlds (N. Madhusudhan, A. A. A. Piette & S. Constantinou 2021) and temperate sub-Neptunes (S. Seager et al. 2021), could contain environments that satisfy a range of habitability requirements, which at present remain poorly understood. By broadening parameters associated with habitability, a wider range of planetary conditions can be encompassed, thus enabling more diverse interpretations of where life might exist beyond Earth.

In the era of *James Webb Space Telescope* (*JWST*; J. P. Gardner et al. 2006; The *JWST* Transiting Exoplanet Community Early Release Science Team et al. 2022; J. P. Gardner et al. 2023), feasible exoplanet atmospheric characterization observations are limited not only by the amplitude of atmospheric features, by also by the frequency with which repeated observations can be obtained. The low stellar luminosities of mid-to-late-type M dwarfs place their temperate zones at short orbtial periods, and their small radii allow for relatively deep transits even from small planets (see e.g. A. H. M. J. Triaud et al. 2013a). These factors make temperate planets around nearby bright late-type M dwarfs among the most favourable *JWST* targets, allowing for high signal-to-noise ratio (SNR) detections of key atmospheric features with only a few hours of telescope time (D. Charbonneau & D. Deming 2007; C. V. Morley et al. 2017).

This paper increases this small, but growing sample of planets with both Earth- and Neptune-sized exoplanets orbiting mid-to-late-type M dwarfs. While these planets are not in the HZ, they sit at the inner (hotter) edge of the temperate zone, facilitating studies of how different types of warm planets form and evolve around fully convective M dwarfs, i.e. in systems with environments much different from the environment in our own Solar system. In this work we also introduce a survey designed to produce a catalogue of precise radii for temperate planets orbiting late-type M ($\leq$ 3400 K) dwarfs using the SPECULOOS (Search for habitable Planets EClipsing ULtra-cOOl Stars; D. Sebastian et al. 2021; S. Zúñiga-Fernández et al. 2025), described in Section 3.

Our paper is organized as follows: first, we start with defining the temperate zone in Section 2, followed by an introduction to the TEMPOS survey in Section 3. In Section 4, we characterize the host stars using reconnaissance spectroscopy and their spectral energy distributions (SEDs). Next, we describe the identification of the planet candidates from *TESS* data in Section 5. Section 6 outlines the methods to validate the planet candidates, and describes our ground-based follow-up efforts that contribute to this. We then describe the global analysis of all photometric data for each planet in Section 7, followed by a discussion and conclusion of our results in Section 8.

2 DEFINITION OF THE 'TEMPERATE ZONE'

Throughout the exoplanet literature, especially in the context of small and potentially habitable planets, we encounter the word 'temperate'. In general, each work makes it clear how they define this term. For instance, M. Greklek-McKeon et al. (2025), presenting the TOI-1266 system, define 'temperate' to mean having an equilibrium below 450 K. This definition includes both transiting planets in this system, the inner of which has $T_{\rm eq} = 415$ K and instellation flux of 4.72 $S_\oplus$. However, J. Yang & R. Hu (2024) define 'temperate sub-Neptunes' as those having $T_{\rm eq} \lesssim 500$ K. 'Temperate' is stated to mean an equilibrium temperature of 400 K in T. Encrenaz et al. (2022) and A. A. A. Piette, N. Madhusudhan & A. M. Mandell (2022), while in M. S. Peterson et al. (2023) it is defined as < 400 K. In this latter work, the 'temperate' planet LP 791-18 d is presented, with $T_{\rm eq} = 395.5$ K and instellation flux of 5.83 $S_\oplus$. In M. N. Günther et al. (2019) TOI-270 d is presented as a 'temperate' 2.13 $R_\oplus$ planet with a $T_{\rm eq} = 387$ K and an instellation flux of 3.92 $S_\oplus$. Here 'temperate' is defined as the having equilibrium temperatures between the survival temperature for extremophiles (395 K) and the freezing point of water (273.15 K).

We also find that several works describe a planet as 'temperate' without giving a specific definition. Examples include HD 35 843 c, a 'temperate' 2.54 $R_\oplus$ planet with a $T_{\rm eq} = 479$ K and an instellation flux of 11.38 $S_\oplus$ (K. Hesse et al. 2025), while TOI-2285 b is reported as a 'venus-zone temperate' planet with 1.77 $R_\oplus$ and $T_{\rm eq} = 358$ K and instellation flux of 3.91 $S_\oplus$ (A. Fukui 2025; E. L. Miles et al. 2025). Additionally, M. Mallorquín et al. (2023) present the young 'temperate' mini-Neptune TOI-1801 b with a $T_{\rm eq} = 493$ K and instellation flux of 10.73 $S_\oplus$. These planets have similar equilibrium temperatures, but instellation fluxes in the range $3.91 - 11.4$ $S_\oplus$, putting them beyond classical habitability arguments found in works like R. K. Kopparapu et al. (2014).

Some works define a 'temperate zone' in terms of stellar irradiation, as is done for the so-called 'habitable zone'. For instance N. B. Cowan et al. (2015) define 'temperate terrestrial planet' as

[1]NASA exoplanet archive, 2025 June; https://exoplanetarchive.ipac.caltech.edu. Recalculated from quoted stellar luminosities and semimajor axes.

one having 0.5 $R_\oplus$ < R < 1.5 $R_\oplus$ and 0.5 $S_\oplus$ < S < 1.5 $S_\oplus$. On the other hand, S. Seager et al. (2021) define 'temperate' simply to mean receiving 'Earth-like' irradiation flux from a host star, as this could lead to liquid water in the atmosphere or on the surface. A. H. M. J. Triaud et al. (2024) again give a specific instellation range, defining 'temperate' in their work to mean 0.25 $S_\oplus$ < S < 4 $S_\oplus$. We also find that in some works, like A. Reiners et al. (2018) and L. Sun et al. (2025), 'temperate zone' is used interchangeably with 'habitable zone'. R. Wells, K. Poppenhaeger & C. A. Watson (2019) present K2-133 e as a 'temperate zone' planet with a T_{eq} = 296 K and insolation flux of 1.8 $S_\oplus$. They note that the instellation puts it outside the HZ boundaries but they use the Earth Similarity Index (ESI; D. Schulze-Makuch et al. 2011) to assess 'habitability' instead. The ESI is part of a two-tier system to quantify how an Earth-like planet is in terms of its size, density, escape velocity, and mean surface temperature.

And of course, all seven planets in the TRAPPIST-1 system are presented as 'temperate', with equilibrium temperatures 172–398 K and instellation fluxes of $0.14 - 4.15\ S_\oplus$ (M. Gillon 2018). For the inner planets, arguments about potential habitability are centred around the possibility of a localized habitable region on the planets, potentially at the terminator of these tidally locked worlds (K. Menou 2013).

For our work, we seek to formalize the definition of a 'temperate zone' in terms of an instellation range, in a manner that incorporates as many as possible of the above definitions. We queried the NASA Exoplanet Archive for confirmed transiting exoplanets from the Composite Data table having irradiation fluxes < 10 $S_\oplus$. These are plotted in Fig. 1. As 400 and 450 K are the two most common cut-offs we find in the literature for calling a planet 'temperate', we perform a kernel density estimation (KDE) analysis of the instellation flux distribution, restricted to planets with $R_p \leq 4R_\oplus$ and equilibrium temperatures either ≤ 400 K or ≤ 450 K. In each case, we assess the distribution of all planets in the sample, as well as a sample that is further restricted to planets smaller than $1.5R_\oplus$ to see any differences for planets most likely to be rocky. The KDE curves are plotted in the upper panels of Fig. 1.

For the ≤ 400 K, we find median and 75th percentile values of 2.687 $S_\oplus$ and 4.242 $S_\oplus$, respectively, for the $R_p \leq 4\ R_\oplus$ distribution, and 2.214 $S_\oplus$ and 4.205 $S_\oplus$, respectively, for the $R_p \leq$ 1.5 $R_\oplus$ distribution. These values are highlighted on the upper panel of Fig. 1. The corresponding values for median and 75th percentile for the ≤ 450 K sample are $3.914S_\oplus$ and 6.1425 $S_\oplus$, respectively, for the $R_p \leq 4\ R_\oplus$ distribution, and 4.09 $S_\oplus$ and 6.1 $S_\oplus$, respectively, for the $R_p \leq 1.5\ R_\oplus$ distribution. We highlight these values in the middle panel of Fig. 1.

We therefore place our upper boundary of the temperate zone at $S_p = 5\ S_\oplus$, just below the median of the 75th percentiles (5.17 $S_\oplus$). By using the 75th percentiles we ensure that we capture the majority of these temperate planets while excluding the high-irradiation tail of the distributions. We also adopt an upper equilibrium temperature boundary of 400 K, and a lower instellation boundary of $S_p = 0.1\ S_\oplus$ to incorporate the extremes of the TRAPPIST-1 planets.

This definition is both statistical and astrophysical. The upper T_{eq} limit follows M. N. Günther et al. (2019), who motivated it by the 395 K survivability limit of terrestrial extremophiles. Additionally, all seven TRAPPIST-1 planets fall in this regime, where 3D climate models predict that liquid water could exist on tidally locked worlds through dayside cloud feedback (J. Yang, N. B. Cowan & D. S. Abbot 2013) or terminator habitability (K. Menou 2013; A. H. Lobo et al. 2023). Thus our 'temperate zone' definition extends the classical habitable zone concept beyond the limits defined by R. K. Kopparapu et al. (2014) to incorporate a wider diversity of potentially clement worlds.

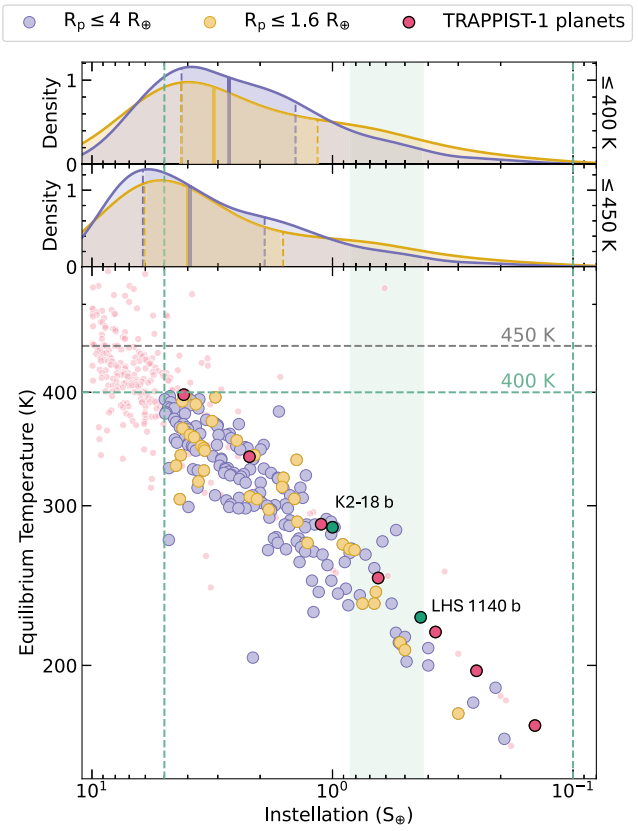

Figure 1. Our adopted definition of the temperate zone. In the lower panel we plot transiting planets retrieved from the NASA Exoplanet Archive in terms of equilibrium temperature and instellation. The small pink points in the foreground represent the full sample, darker purple points have $R_p \leq 4\ R_\oplus$, and lighter brown points have $R_p \leq 1.5\ R_\oplus$. The seven temperate planets of the TRAPPIST-1 system are shown as red, outlined points, and in green outline we highlight K2-18 b and LHS 1140 b, two canonical temperate planets. The green shaded area indicates the conservative habitable zone as defined by R. K. Kopparapu et al. (2014); the temperate zone is enclosed by the green dashed lines. The two upper panels show the KDE curves for the planet samples, with the colours matching the points in the lower panel.

3 TEMPOS: TEMPERATE M DWARF PLANETS WITH SPECULOOS

As described briefly in Section 1, this paper aims to introduce for the first time a programme running on the SPECULOOS telescopes, TEMPOS (**TE**mperate **M** dwarf **P**lanets with SPECULO**OS**). This programme aims to produce a catalogue of precise temperate exoplanet radii for planets transiting mid- to late-type M dwarfs. Ultimately, we aim to achieve precisions $\lesssim$ 3 per cent (*PLATO* goal, H. Rauer et al. 2025), but have a minimum requirement of at least < 7 per cent.

All targets in our TEMPOS sample are obtained from the *TESS* Objects of Interest (TOIs) list. We retain TOIs that meet the following criteria: $T_{eff} \leq 3400$ K, $0.1 \leq S/S_\oplus \leq 5$, and are confirmed planets or planet candidates. This sample is not planet-radius

limited. At the time of writing, the TEMPOS sample contains 40 confirmed or candidate planets (21 and 19, respectively). For the confirmed planets, we update the TOI parameters with published values.

From the available planet radii in this sample, we find current mean and median precisions of 21.3 per cent and 7.7 per cent, respectively. Fewer than half of these planets (19) have precisions less than our minimum target threshold of 7 per cent, 13 of which are confirmed planets. In total, only two planets (both confirmed) have precisions ≤ 3 per cent.

Why require a planetary radius precision of ≤ 7 per cent, with a goal of ≤ 3 per cent? Many studies require precisely measured exoplanet radii (see e.g. L. Parc et al. 2024), especially since exoplanet masses are typically much less precise (average precision > 20 per cent[2]). A radius precision below 7 per cent is sufficient for exoplanet population-level studies and for selecting targets for atmospheric follow-up with *JWST*.

For smaller planets ($\leq 2\,R_\oplus$), however, a higher precision is crucial. A ~ 3 per cent uncertainty is typically needed to distinguish between purely rocky planets and those with volatile envelopes. For example, L. A. Rogers (2015) show that a $R_p = 1.6\,R_\oplus$ planet with a 5 per cent uncertainty could sit either side of the radius valley, at either $R_p = 1.5\,R_\oplus$ or $R_p = 1.7\,R_\oplus$. The radius valley is defined as the observed dearth in close-in ($P < 100$ d) exoplanets with radii in the range $1.5\,R_\oplus < R_p < 2\,R_\oplus$ (B. J. Fulton et al. 2017), and is thought to separate terrestrial super-Earths and gaseous sub-Neptunes, potentially through mechanisms such as photoevaporation of primordial H/He atmospheres (e.g. H. Chen & L. A. Rogers 2016; J. E. Owen & Y. Wu 2017), core-powered mass-loss (A. Gupta & H. E. Schlichting 2019), or 'gas-poor' formation (E. D. Lopez & K. Rice 2018). Thus, a planet with a 5 per cent radius uncertainty could be classified as either a super-Earth or sub-Neptune. Therefore, in order accurately distinguish between these compositions, we adopt a target precision of 3 per cent on planet radius, which matches the *PLATO* mission goals. While a ~ 7 per cent precision does not necessarily allow for finer differentiation between planet compositions, it is sufficient for robust statistical studies of small planet demographics.

4 STELLAR CHARACTERIZATION

TOI-6716 (TIC 112115898) and TOI-7384 (TIC 192833836) are two M dwarfs of spectral type M4, located at 18.9 and 66.8 pc from the Sun, respectively (C. A. L. Bailer-Jones et al. 2021). As all our planetary information will be derived using the host stars' parameters, we begin in the sections that follow by characterizing TOI-6716 and TOI-7384. All photometric and stellar parameters adopted for this work can be found in Table 1.

4.1 Reconnaissance spectroscopy

4.1.1 TOI-6716

We observed TOI-6716 with the Kast double spectrograph (J. S. Miller & R. P. S. Stone 1994) on the 3-m Shane telescope at Lick Observatory on 2025 March 8 (UT) in clear conditions with 1.2 arcsec seeing. We used the 1.5 arcsec slit aligned to the parallactic angle to obtain blue and red optical spectra split at 5700 Å by the d57 dichroic, and dispersed by the 600/4310 grism and 600/7500 grating, resulting in spectral resolutions of $\lambda/\Delta\lambda \approx 1100$ and ≈ 1500 for the blue and red spectra, respectively. We obtained a single 500 s exposure in the blue channel and two 250 s exposures in the red channel at an average airmass of 2.7. The G2 V star HD 60 513 ($V = 6.7$) was observed at a slightly lower airmass of 2.0 for telluric absorption calibration, and the spectrophotometric calibrator Hiltner 600 (M. Hamuy et al. 1992, 1994) was observed shortly thereafter for flux calibration. We used HeHgCd and HeNeArHg arc lamp exposures to wavelength calibrate our blue and red data, and flat-field lamp exposures for pixel response calibration. Data were reduced using the `kastredux` code[3] using standard settings. The resulting spectra have median SNRs of 22 at 5425 Å and 88 at 7350 Å.

The reduced spectrum is shown in Fig. 2, with a comparison to the best-fitting M4 dwarf SDSS spectral template from J. J. Bochanski et al. (2007). This classification was confirmed using index-based methods described in I. N. Reid, S. L. Hawley & J. E. Gizis (1995), J. E. Gizis (1997), E. L. Martín et al. (1999), S. Lépine, R. M. Rich & M. M. Shara (2003), and F. C. Riddick, P. F. Roche & P. W. Lucas (2007), which span M3 to M4. We detect a weak signature of H α emission at 6563 Å with an equivalent width EW $= -1.20 \pm 0.18$ Å, corresponding to $\log(L_{H\alpha}/L_{bol}) = -4.37 \pm 0.09$ using the χ factor relation of S. T. Douglas et al. (2014). The presence of weak H α emission indicates an activity age of no more than 4–6 Gyr (A. A. West et al. 2008), while the absence of detectable Li I absorption at 6708 Å rules out a substellar mass and age less than ~ 30 Myr. We measure the metallicity index $\zeta = 1.124 \pm 0.005$ (S. Lépine et al. 2013), which corresponds to a roughly solar metallicity of [Fe/H]$= +0.17 \pm 0.20$ using the A. W. Mann et al. (2013) calibration, consistent with solar metallicity.

We also observed TOI-6716 with the SpeX spectrograph (J. T. Rayner et al. 2003) on the 3.2-m NASA Infrared Telescope Facility (IRTF) on 2024 November 10 (UT) under clear conditions with 0.5 arcsec seeing. Using the short-wavelength cross-dispersed (SXD) mode and the 0.3 arcsec × 15 arcsec slit ($\lambda/\Delta\lambda \sim 2000$, 0.80–2.42 μm) aligned to the parallactic angle, we obtained eight 60-s exposures at an airmass of 1.6, nodding in an ABBA pattern. We followed with a standard set of SXD flat field and arc lamp calibrations and 12 30-s exposures of the A0 V standard HD 56751 (V=7.1) at a similar airmass. Data reduction with the Spextool v4.1 pipeline (M. C. Cushing, W. D. Vacca & J. T. Rayner 2004) followed the standard approach (K. Barkaoui et al. 2024; M. Ghachoui et al. 2024; K. Barkaoui et al. 2025). The final spectrum has a median SNR per pixel of 144.

The SXD spectrum of TOI-6716 is shown in Fig. 3. With respect to single-star standards in the IRTF Spectral Library (M. C. Cushing, J. T. Rayner & W. D. Vacca 2005; J. T. Rayner, M. C. Cushing & W. D. Vacca 2009), we find the closest match to the M4 V standard Ross 47 using the SpeX Prism Library Analysis Toolkit (SPLAT; A. J. Burgasser & Splat Development Team 2017) and adopt a spectral type of M4.0 ± 1.0, consistent with the optical classification. From the K-band Na I and Ca I lines and the H_2O–K2 index (B. Rojas-Ayala et al. 2012), we estimate [Fe/H] $= -0.09 \pm 0.12$ using the A. W. Mann et al. (2013) relation and the Monte Carlo approach detailed previously (L. Delrez et al. 2022; M. Ghachoui et al. 2023), again consistent with solar metallicity.

[2]NASA exoplanet archive, 2025 July.

[3]https://github.com/aburgasser/kastredux.

Table 1. Stellar parameters adopted for this work.

Star	TOI-6716	TOI-7384	
Designations	TIC 112115898, 2MASS J07263809-3033087, *Gaia* DR2 5605438925569442432, UCAC4 298–022880	TIC 192833836, 2MASS J05322483-3950016, *Gaia* DR2 4808732662634331520, UCAC4 251–006761, WISE J053224.78-395002.7	
Parameter	Value	Value	Source
T mag	11.774±0.007	13.694±0.008	K. G. Stassun et al. (2019)
B mag	16.362±0.061	17.63±0.17	N. Zacharias et al. (2013)
V mag	14.8±0.2	16.704±0.206	N. Zacharias et al. (2013)
G mag	13.1269±0.0006	15.0456±0.0008	Gaia Collaboration (2022)
J mag	10.093±0.026	12.001±0.026	R. M. Cutri et al. (2003)
H mag	9.535±0.026	11.382±0.026	R. M. Cutri et al. (2003)
K mag	9.196±0.021	11.096±0.023	R. M. Cutri et al. (2003)
W1 mag	–	10.942±0.023	R. M. Cutri et al. (2021)
W2 mag	–	10.779±0.021	R. M. Cutri et al. (2021)
W3 mag	–	10.551±0.064	R. M. Cutri et al. (2021)
W4 mag	–	> 8.92	R. M. Cutri et al. (2021)
Distance	18.89±0.02 pc	66.79±0.20 pc	C. A. L. Bailer-Jones et al. (2021)
α	07:26:37.7	05:32:24.76	Gaia Collaboration (2022)
δ	−30:33:07.85	−39:50:03.3	Gaia Collaboration (2022)
μ_α	-316.5 mas yr^{-1}	-46.0 mas yr^{-1}	Gaia Collaboration (2022)
μ_δ	59.0 mas yr^{-1}	-101.8 mas yr^{-1}	Gaia Collaboration (2022)
SpT	M4	M4	This work (opt. spec.)
	M4	M3±0.5	This work (NIR spec.)
$R_\star$	0.231 ± 0.015 R$_\odot$	0.319 ± 0.018 R$_\odot$	This work (SED)
$M_\star$	0.223 ± 0.0110 M$_\odot$	0.318 ± 0.016 M$_\odot$	This work (SED)
T$_{\rm eff}$	3110±80 K	3185±75 K	This work (SED)
log $g_\star$	5.06±0.06	4.93±0.05	This work (from SED)
[Fe/H]	0.0±0.5 dex	0.0±0.5 dex	This work (SED)
	+ 0.17±0.20 dex	+ 0.17±0.20 dex	This work (opt. spec.)
	−0.09±0.12 dex	+ 0.18±0.11 dex	This work (NIR spec.)

4.1.2 TOI-7384

We gathered an optical spectrum of TOI-7384 using the Low Dispersion Survey Spectrograph (LDSS-3C; K. B. Stevenson et al. 2016) on the 6.5-m *Magellan II* (Clay) Telescope on 2022 January 7 (UT) during clear conditions with 0.5 arcsec seeing. We used the standard set-up for the long-slit mode (fast readout speed, low gain, and 1×1 binning) along with the VPH-Red grism, OG-590 blocking filter, and the 0.75 arcsec × 0.4 arcsec centre slit. This configuration provides spectra covering 6000–10 000 Å with a spectral resolving power of R∼1810. We collected six, 300-s exposures at an average airmass of 1.023. We followed the science observations with three, 1-s exposures of the F8 V star HR 1651 (R. O. Gray et al. 2006). At each pointing, we collected a 1-s HeNeAr arc lamp exposure and three 10-s flats with the 'quartz high' lamp. We used a custom Python-based pipeline (G. Dransfield et al. 2023) to reduce the data, including bias removal, flat-field correction, and spectral extraction. We used the HeNeAr arc exposure for wavelength calibration. While we did not apply a telluric correction, we used the ratio of the F8 V spectrum to the F8 V template from A. J. Pickles (1998) to calculate a relative flux correction. The final spectrum has a maximum SNR per pixel of 177 at 9183 Å, a mean SNR per pixel of 113 in the 6000–10 000 Å range, and an average of 2.3 pixels per resolution element.

The LDSS-3 spectrum of TOI-7384 is also shown in Fig. 2, also compared to its best-fitting M4 dwarf SDSS spectral template, which is again consistent with index-based classifications spanning M3.5–M4.5. We detect Hα in absorption in this spectrum (EW = + 1.12±0.17 Å) indicating weak or absent magnetic activity and an activity age of at least 4.5 Gyr (A. A. West et al. 2008). For this source we measure $\zeta = 1.127 \pm 0.003$, which again corresponds to a roughly solar metallicity of [Fe/H]= $+0.17 \pm 0.20$ using the A. W. Mann et al. (2013) calibration.

We also observed TOI-7384 with the FIRE spectrograph (R. A. Simcoe et al. 2008) on the 6.5-m Magellan Baade Telescope on 2023 February 2 (UT) under clear conditions with 1.0 arcsec seeing. We used the high-resolution echellette mode with the 0.45 arcsec slit, providing 0.9–2.4 μm spectra with a resolving power of R∼8000. We collected two exposures of 306.5-s each, nodding between frames. Following the science observations, we collected a 30-s arc lamp exposure and two, dithered exposures of the A0 V standard HD 38433 (V=9.4). Along with a set of internal and dome flats collected the previous afternoon, we used these calibrations to reduce the data with the `FIREHOSE` pipeline.[4] The final spectrum has a median SNR per pixel of 151 and an average of 2.4 pixels per resolution element.

The FIRE spectrum of TOI-7384 is shown in Fig. 3. We used SPLAT to compare the spectrum to SXD spectra of single-star standards in the IRTF Spectral Library (M. C. Cushing et al. 2005; J. T. Rayner et al. 2009). We found the best spectral match to the M3.5 standard GJ 273 with similar but poorer matches to the M3 standard GJ 388 and M4 standard GJ 213, and so we adopt an infrared spectral type of M3.5 ± 0.5, again consistent with the optical type. To address an issue with continuum normalization at the long-wavelength end of the spectrum, we applied a correction

[4] https://github.com/rasimcoe/FIREHOSE

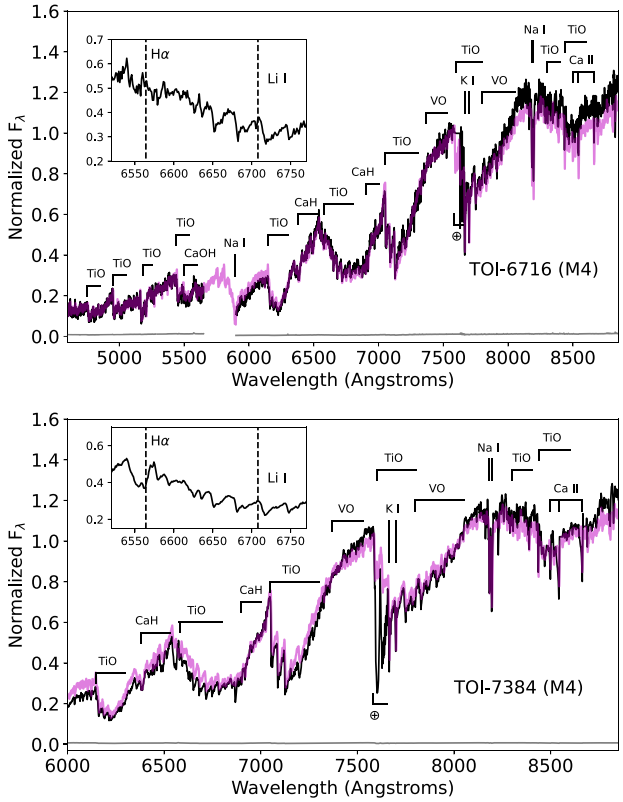

Figure 2. Shane/Kast optical spectrum of TOI-6716 (top) and Magellan/LDSS-3 spectrum of TOI-7384 (bottom), compared to their best-fitting M4 SDSS spectral template from J. J. Bochanski et al. (2007, magenta (lighter-coloured) line). Key spectral features are labelled, including regions of residual telluric absorption (⊕). Inset boxes show the 6520–6770 Å region encompassing H α and Li I features. The gap in the Kast spectrum between 5600 and 5900 Å corresponds to the gap between that instrument's blue and red channels.

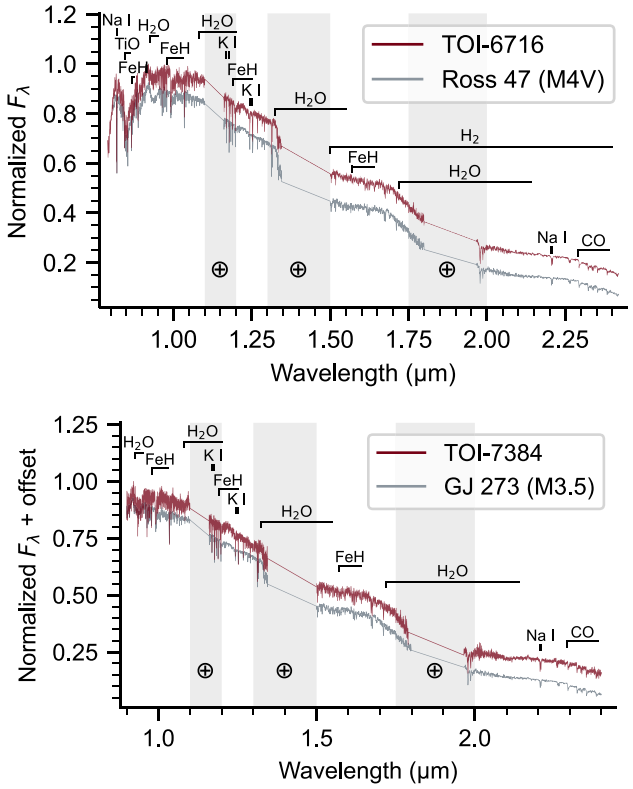

Figure 3. SpeX/SXD spectrum of TOI-6716 (top) and Magellan/FIRE spectrum of TOI-7384 (bottom). The target spectra (red, darker line) are compared to M4V standard Ross 47 and the M3.5 standard GJ 273, respectively, both shown in grey (lighter line) and offset vertically. Strong M-dwarf spectral features and spectral regions with strong telluric absorption are indicated.

to the data at wavelengths >2.25 μm using the spectrum of GJ 273 as a reference. We used the corrected spectrum to estimate the stellar metallicity using the A. W. Mann et al. (2013) relation between the equivalent widths of the *K*-band Na I and Ca I doublets and the H2O–K2 index (B. Rojas-Ayala et al. 2012). This gives an iron abundance of [Fe/H] = +0.18 ± 0.11, consistent with the optical metallicity.

4.2 Spectral energy distribution

As an independent determination of the basic stellar parameters, we performed an analysis of the broad-band SED of each of the stars together with the *Gaia* DR3 parallax (with no systematic offset applied; see e.g. K. G. Stassun & G. Torres 2021). This yielded, upon following the procedures described in K. G. Stassun & G. Torres (2016), K. G. Stassun, K. A. Collins & B. S. Gaudi (2017), and K. G. Stassun et al. (2018), an emperical measurement of each stellar radius. We pulled the the JHK_S magnitudes from *2MASS*, the W1–W3 magnitudes from *WISE*, and the $G_{BP}G_{RP}$ magnitudes from *Gaia*. Finally, we utilized the absolute flux-calibrated *Gaia* spectrophotometry where available. Together, the available photometry spans the full stellar SED over the wavelength range 0.4–10 μm (see Fig. 4).

We performed a fit using NextGen stellar atmosphere models (P. H. Hauschildt, F. Allard & E. Baron 1999), with the free parameters being the effective temperature ($T_{\rm eff}$) and metallicity ([Fe/H]), as well as the extinction A_V, which we limited to maximum line-of-sight value from the Galactic dust maps of D. J. Schlegel, D. P. Finkbeiner & M. Davis (1998). Integrating the (unreddened) model SED gives the bolometric flux at Earth, $F_{\rm bol}$. Taking the $F_{\rm bol}$ and $T_{\rm eff}$ together with the *Gaia* parallax gives the stellar radius, $R_\star$. In addition, we can estimate the stellar mass from the empirical M_K relations of A. W. Mann et al. (2019). For TOI-6716 b, the resulting fit (Fig. 4) has a best fit $A_V \equiv 0$, $T_{\rm eff} = 3110 \pm 80$ K, [Fe/H] = 0.0 ± 0.5, with a reduced χ^2 of 2.2. Thus, we find $F_{\rm bol} = 4.027 \pm 0.094 \times 10^{-10}$ erg s^{-1} cm^{-2}, $R_\star = 0.231 \pm 0.015$ R$_\odot$, and $M_\star = 0.223 \pm 0.011$ M$_\odot$. For TOI-7384 b, the resulting fit (Fig. 4) has a best fit $A_V = 0.01 \pm 0.01$, $T_{\rm eff} = 3185 \pm 75$ K, [Fe/H] = 0.0 ± 0.5, with a reduced χ^2 of 1.9. Thus, we find $F_{\rm bol} = 6.75 \pm 0.40 \times 10^{-11}$ erg s^{-1} cm^{-2}, $R_\star = 0.319 \pm 0.018$ R$_\odot$, and $M_\star = 0.318 \pm 0.016$ M$_\odot$.

While a set of stellar parameters may also be obtained using empirical relations, we choose to use those calculated from the SED. This choice is motivated by the fact that empirical relations rely on the *Gaia* DR3 *BP-RP* colour to estimate the $T_{\rm eff}$, which is known to be unreliable for cooler stars (see e.g. C. Jordi et al. 2010), and is highly sensitive to metallicity, which is challenging to robustly derive for M dwarfs (see e.g. S. Lindgren & U. Heiter 2017; V. M. Passegger et al. 2022). In contrast, the SED fitting

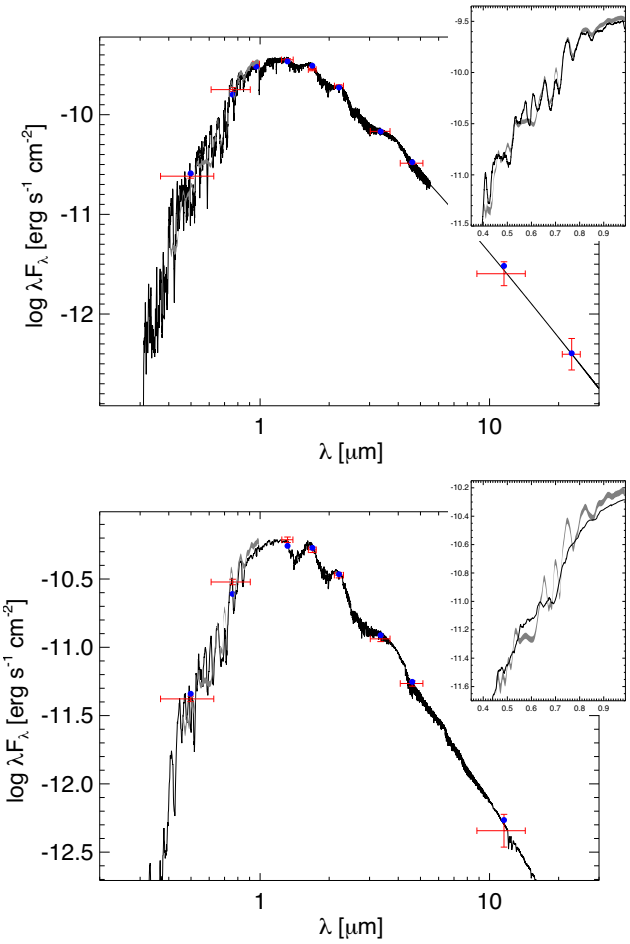

Figure 4. SEDs of TOI-6716 (top) and TOI-7384 (bottom). The red symbols represent the observed photometric measurements, where the horizontal bars represent the effective width of the passband. The blue symbols are the model fluxes from the best-fitting NextGen atmosphere model (black). The inset axes show the absolute flux-calibrated *Gaia* spectrophotometry as a grey swathe overlaid on the best-fitting model.

approach uses a wide range of broad-band photometry and allows both $T_{\rm eff}$ and metallicity to be free parameters. The resulting stellar parameters derived from this are thus more robust and have more conservative uncertainties.

5 PLANET IDENTIFICATION

5.1 Candidate identification

Prior to TOI-7384 b being identified as a planet candidate by *TESS*, observations were first triggered by the NEMESIS (Exoplanet Tra**N**sit Survey of N**E**arby **M** Dwarfs in *T* **ES** *S* FF**Is**) pipeline, presented in D. L. Feliz et al. (2021). This pipeline was designed to produce detrended photometry of M dwarfs visible in *TESS* full-frame images (FFIs) and conduct a transit search on the resulting light curves. In the first release the pipeline analysed *TESS* data from Sectors 1–5, which included 33 054 M dwarfs within 100 pc, and produced 29 planet candidates. Of these, five matched known TOIs and the remaining 24 were new detections. We selected the 12 candidates found orbiting the hosts with effective temperatures < 3300 K as these aligned the best with the existing SPECULOOS target list. These were given internal designations of NEMESIS 1–12 for the purpose of our follow-up campaign. Nemesis-12 was identified as a planet candidate and designated the CTOI (Community *TESS* Object of Interest) TIC 192833836.01. In 2025 April, it was identified as TOI-7384.01, which will remain its designation throughout this paper.

TOI-6716 was observed in *TESS* FFIs at cadence 1800 s in Sector 7, 600 s in Sector 34, 200 s in Sectors 61, 87, and 88, 120 s in Sectors 7, 34, 61, 87, and 88, and 20 s in Sectors 87 and 88. It was reported as a planet candidate on 2023 October 5. Fig. 5 shows the *TESS* 120 s cadence photometric observations reduced by the SPOC (Science Processing Operations Center) pipeline (J. M. Jenkins et al. 2016). It has a candidate orbital period and planetary radius of $P_{b,\,6716} = 4.72$ d and $R_{b,\,6716} = 1.01\,{\rm R}_\oplus$, respectively. TOI-7384 was observed in *TESS* FFIs in Sectors 5 (as mentioned above) and 6 in 1800 s cadence, 32 and 33 in 600 s cadence, and 87 in 200 and 120 s cadence. In Fig. 6 we present the *TESS* photometry as reduced by the TESS-SPOC (Sectors 5,6,32,33) and SPOC (Sector 87) pipelines. TOI-7384 b has a candidate orbital period and planetary radius of $P_{b,\,7384} = 6.23$ d and $R_{b,\,7384} = 3.93\,{\rm R}_\oplus$, respectively. The data for both TOI-6716 and TOI-7384 are available on the NASA Mikulski Archive for Space Telescopes.

We use the python package TPFPLOTTER[5] (A. Aller et al. 2020) to plot the field of view around each star along with the *TESS* apertures from their most recent *TESS* sectors at the time of writing; these are shown in Fig. 7. We can conclude that there is no significant contamination from bright sources in or near the target stars/*TESS* aperture, which could be either diluting our transit event, or be the source of the transit event itself. This is discussed further in Section 6.5.

5.2 Search for additional candidates and detection limits

We used the custom pipeline SHERLOCK[6] (see e.g. B. O. Demory et al. 2020; F. J. Pozuelos et al. 2020) to analyse the TESS data described in Section 5.1. This has the dual aims of independently recovering TOI-6716 b and TOI-7384 b, and searching for additional planetary candidates potentially overlooked by official pipelines such as SPOC and QLP due to their detection thresholds. The SHERLOCK pipeline is specifically designed to identify low-SNR transit-like signals indicative of planetary transits. It integrates various modules that facilitate data access and rapid inspection, automated transit searches, candidate vetting and validation, Bayesian modelling to derive precise planetary parameters and ephemerides, and the computation of observational windows to guide follow-up campaigns (M. Dévora-Pajares et al. 2024). We successfully recovered the previously known TOI alerts in our initial runs but did not detect any additional transit-like features attributable to planetary origins.

The lack of additional detections may result from several possibilities (see e.g. N. Schanche et al. 2021; R. D. Wells et al. 2021; F. J. Pozuelos et al. 2023): the system may not contain any additional transiting planets with orbital periods within the range explored here (≤ 10 d), any additional transiting planets, or even any any additional planets. Alternatively, additional transiting planets may remain undetected due to the limited photometric precision of the data. To assess this possibility, we conducted

[5]TPFPLOTTER is publicly available at https://github.com/jlillo/tpfplotter.
[6]SHERLOCK is publicly available at https://github.com/franpoz/SHERLOCK.

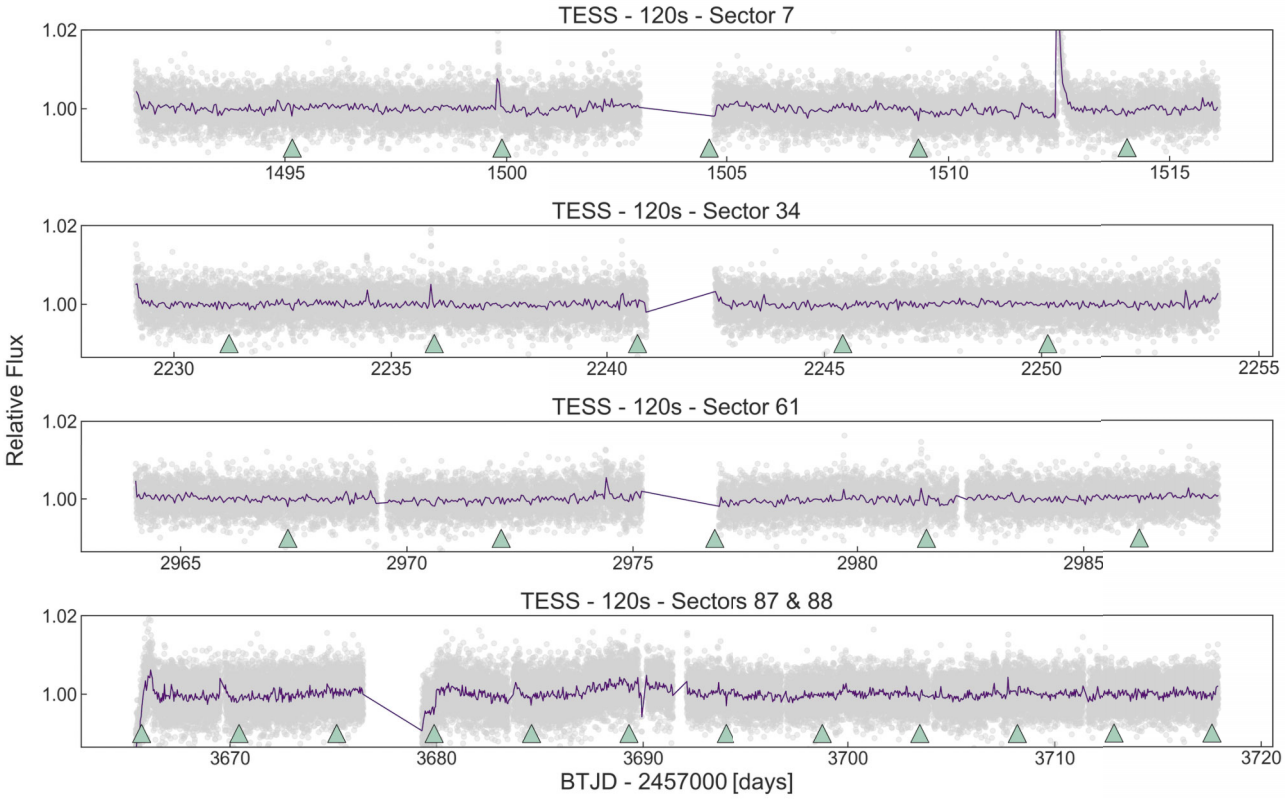

Figure 5. *TESS* 2-min cadence photometry (grey) for TOI-6716 for Sectors 7 (top), 34 (top-middle), 61 (bottom-middle), 87, and 88 (bottom). Purple solid line shows the data binned by 1 h. Transits are indicated with green triangles, although are not visually obvious in the *TESS* data.

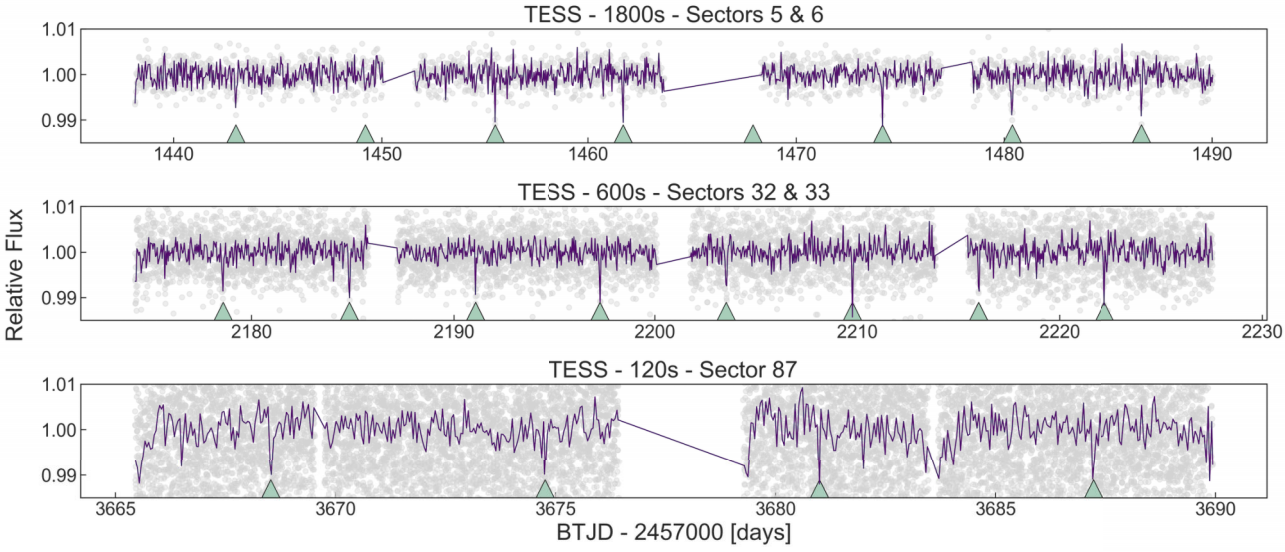

Figure 6. *TESS* photometry (grey) for TOI-7384 in 2-min cadence (top), 10-min cadence (middle), and 30-min cadence (bottom). Purple solid line shows the data binned by 1 h. Transits are indicated with green triangles.

injection-and-recovery tests with the MATRIX code[7] (M. Dévora-Pajares & F. J. Pozuelos 2022).

[7]The MATRIX (**M**ulti-ph**A**se **T**ransits **R**ecovery from **I**njected e**X**oplanets) code is open access on GitHub: https://github.com/PlanetHunters/tkmatrix.

The code explores a three-dimensional parameter space (orbital period, planetary radius, and transit epoch) by generating a grid of synthetic scenarios, which are injected into the original light curve. In our case, the grid comprises 30 periods, 30 radii, and 5 epochs, resulting in 4500 different scenarios. A synthetic planet is considered as retrieved when a period and an epoch are

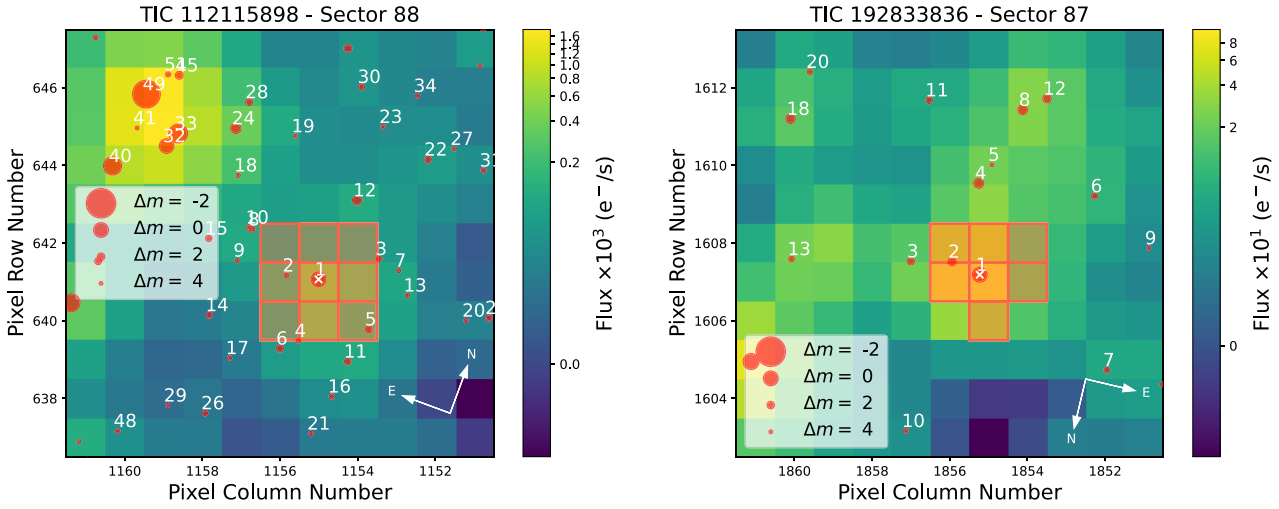

(a) Target pixel file image for TOI-6716.

(b) Target pixel file image for TOI-7384.

Figure 7. *TESS* target pixel file image created with TPFPLOTTER for TOI-6716 (*left*) and TOI-7384 (*right*) observed in Sector 88 (2025 January 14–2025 February 11) and Sector 87 (2024 December 18–2025 January 14), respectively. The target stars are indicated by a white cross, and the *TESS* aperture is represented by the red hatch. The red dots highlight *Gaia*-DR3 sources with varying sizes corresponding to their magnitude relative to the respective target stars.

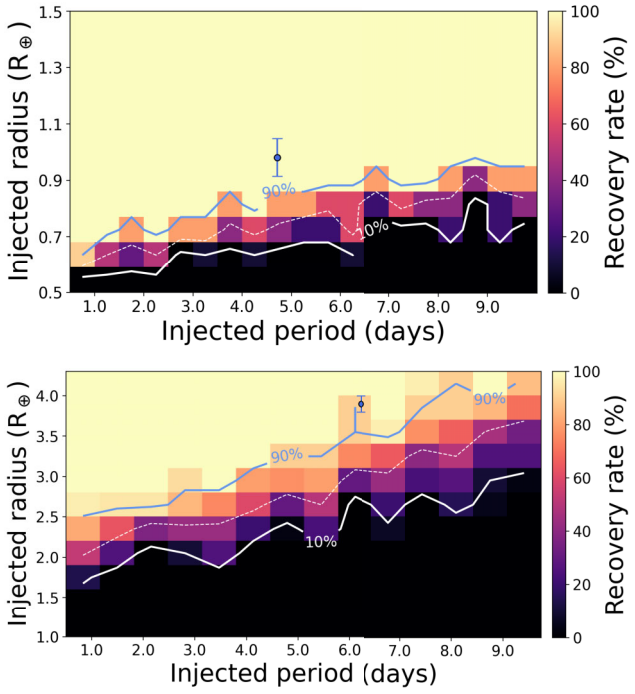

Figure 8. Injection-and-recovery experiment performed to establish the detection limits using all the available *TESS* sectors in each case. Colour code indicates recovery rate: bright yellow for high recovery, dark purple/black for low recovery. The solid blue line indicates the 90 per cent recovery contour, the dashed white line marks the 50 per cent, and the solid white line corresponds to the 10 per cent. The blue dots correspond to planets TOI-6716 b (top) and TOI-7384 b (bottom).

found that differ by at most 1 per cent and up to 1 h from the injected values, respectively.

The results, displayed in Fig. 8, indicate that for TOI-6716, planets as small as 0.6 $R_\oplus$ are detectable only on short orbits ($P \lesssim$ 2 d), with a 100 per cent recovery rate for transiting planets larger than 1.0 $R_\oplus$ and $P \leq 10$ d, effectively ruling out their presence. In contrast, for TOI-7384, the smallest planets recovered with ≥90 per cent rate are ∼2.5 $R_\oplus$ at short periods; Earth-sized planets remain undetectable at any period, and their existence cannot be excluded with the current data.

6 VETTING AND VALIDATION

In this section we describe the results of the multifacility follow-up campaign conducted between 2023 October and 2025 April for TOI-6716 b, and between 2021 April and 2023 February for TOI-7384 b. We begin with the high-resolution imaging observations, and then outline the photometric observations collected from SPECULOOS Southern Observatory (SSO), TRAPPIST-South, and LCO. Finally, we describe how all our follow-up observations were used to validate the planetary natures of TOI-6716 b and TOI-7384 b.

All follow-up observations are summarized in Tables 2 and 3.

6.1 Archival imaging

In order to check for a potential blend with our target stars and background objects, we make use of various archival images available to us and compare to images taken from recent ground-based observations. These are shown in Fig. A1 for TOI-6716 (top) and TOI-7384 (bottom). This investigation is made possible by the stars' large proper motion ($PM_{6716} = 322$ mas yr^{-1}, $PM_{7384} = 112$ mas yr^{-1}; Gaia Collaboration 2022), and is a crucial step in assessing whether the observed transit events happen on blended sources.

For TOI-6716, we examined archival imaging spanning 69 yr – from a 1956 red DSS/POSS-I plate through blue (1980) and red (1995) DSS/POSS-II/UKSTU plates and compared them with recent SPECULOOS-South observations. No background source is present at the star's current position. We perform the same analysis for TOI-7384, using a DSS/POSS-II/UKSTU blue plate

Table 2. Summary of ground-based follow-up observations carried out for TOI-6716.

TOI-6716 follow-up observations				
High-resolution imaging				
Observatory	**Filter**	**Date**	**Sensitivity limit**	**Result**
Gemini South	562 nm		$\Delta m = 4.6$ at 0.5 arcsec	No sources detected
Gemini South	832 nm		$\Delta m = 7.0$ at 0.5 arcsec	No sources detected
Photometric follow-up				
Observatory	**Filter**	**Date**	**Coverage**	**Result**
LCO-CTIO−1m0/SINISTRO	*Sloan-i′*	2023 Oct 28	Full	Detection
LCO-SSO-M4/MUSCAT4	*Sloan-g′*	2023 Dec 28	Full	Detection
LCO-SSO-M4/MUSCAT4	*Sloan-r′*	2023 Dec 28	Full	Detection
LCO-SSO-M4/MUSCAT4	*Sloan-i′*	2023 Dec 28	Full	Detection
LCO-SSO-M4/MUSCAT4	z_s	2023 Dec 28	Full	Detection
LCO-HAL-M3/MUSCAT3	*Sloan-g′*	2024 Feb 4	Full	Detection
LCO-HAL-M3/MUSCAT3	*Sloan-r′*	2024 Feb 4	Full	Detection
LCO-HAL-M3/MUSCAT3	*Sloan-i′*	2024 Feb 4	Full	Detection
LCO-HAL-M3/MUSCAT3	z_s	2024 Feb 4	Full	Detection
SSO-Europa	*Sloan-r′*	2025 Apr 3	Full	Detection
Spectroscopic observations				
Instrument	**Wavelength range**	**Date**	**Number of spectra**	**Use**
Shane/Kast	450–900 nm	2025 Mar 8	1	Stellar characterization
IRTF/SpeX	800–2420 nm	2024 Nov 10	1	Stellar characterization

Table 3. Summary of ground-based follow-up observations carried out for TOI-7384.

TOI-7384 follow-up observations				
High-resolution imaging				
Observatory	**Filter**	**Date**	**Sensitivity limit**	**Result**
Gemini South	562 nm		$\Delta m = 5.6$ at 0.5 arcsec	No sources detected
Gemini South	832 nm		$\Delta m = 5.4$ at 0.5 arcsec	No sources detected
Photometric follow-up				
Observatory	**Filter**	**Date**	**Coverage**	**Result**
TRAPPIST-South	$I + z'$	2021 Sept 19	Full	Detection
SSO-Callisto	$I + z'$	2021 Oct 14	Full	Detection
SSO-Ganymede	*Sloan-g′*	2021 Oct 14	Full	Detection
TRAPPIST-South	$I + z'$	2022 Apr 13	Full	Detection
SSO-Io	$I + z'$	2022 Oct 23	Full	Detection
SSO-Callisto	zYJ	2022 Oct 23	Full	Detection
TRAPPIST-South	$I + z'$	2022 Oct 26	Partial	Detection
SSO-Io	*Sloan-g′*	2022 Nov 17	Full	Detection
SSO-Europa	*Sloan-z′*	2022 Nov 17	Full	Detection
SSO-Callisto	zYJ	2022 Nov 17	Full	Detection
SSO-Io	$I + z'$	2022 Dec 12	Full	Detection
SSO-Ganymede	*Sloan-i′*	2023 Jan 6	Full	Detection
SSO-Io	$I + z'$	2023 Jan 6	Full	Detection
SSO-Europa	*Sloan-r′*	2023 Jan 6	Full	Detection
Spectroscopic observations				
Instrument	**Wavelength range**	**Date**	**Number of spectra**	**Use**
Magellan/LDSS3	380–1000 nm	2022 Jan 6	1	Stellar characterization
Magellan/FIRE	380–1000 nm	2023 Feb 2	1	Stellar characterization

taken 47 yr before the 2023 SPECULOOS-South images (1976), along with red (1992) and IR (1996) DSS/POSS-II/UKSTU plates, we reach the same conclusion: no background star is present at the star's current position.

6.2 High-resolution imaging – Zorro

A critical validation and confirmation process for transiting exoplanet observations is to use high-resolution imaging to determine if any close companions exist. The presence of a close com-

panion star, whether truly bound or line of sight, provides 'third-light' contamination of the observed transit, leading to derived properties for the exoplanet and host star that are incorrect (D. R. Ciardi et al. 2015; E. Furlan & S. B. Howell 2017, 2020). Given that nearly one-half of FGK stars are in binary or multiple star systems (R. A. Matson et al. 2018) high-resolution imaging yields crucial information towards our understanding of each discovered exoplanet as well as more global information on exoplanetary formation, dynamics, and evolution (S. B. Howell et al. 2021).

TOI-6716 (TIC 112115898) was observed on 2024 January 2 UT and TOI-7384 (TIC 192833836) was observed on 2022 October 7 UT using the Zorro speckle instrument on the Gemini South 8-m telescope (N. J. Scott et al. 2021). Zorro provides simultaneous speckle imaging in two bands (562 and 832 nm) with output data products including a reconstructed image with robust magnitude contrast limits on companion detections. Five sets of 1000 × 0.06 s images were obtained for TOI-6716 and 15 similar sets were obtained for TOI-7384. All these data were processed with our standard reduction pipeline (S. B. Howell et al. 2011). Fig. B1 shows our final contrast curves and the 832 nm reconstructed speckle images for both stars. We find that TOI-6716 and TOI-7384 are both single stars with no companion brighter than 5–8 and 5–6 mag, respectively, below that of the target star from the Gemini Telescope 8-m telescope diffraction limit (20 mas) out to 1.2 arcsec. At the distance of TOI-6716 ($d = 19$ pc) and TOI-7384 ($d = 67$ pc) these angular limits correspond to spatial limits of 0.38 to 23 au and 1.34 to 80 au, respectively.

6.3 High-resolution imaging – SOAR

We also searched for stellar companions to TOI-6716 with speckle imaging on the 4.1 m Southern Astrophysical Research (SOAR) telescope (A. Tokovinin 2018) on 2024 January 8 UT, observing in Cousins I band, a similar visible bandpass as *TESS*. This observation was sufficiently sensitive to obtain a 5σ detection of a 5.0-mag fainter star at an angular distance of 1 arcsec from the target. More details of the observations within the SOAR *TESS* survey are available in C. Ziegler et al. (2020). The 5σ detection sensitivity and speckle autocorrelation functions from the observations are shown in Fig. C1. No nearby stars were detected within 3 arcsec of TOI-6716 in the SOAR observations.

6.4 Photometric follow-up

6.4.1 SPECULOOS

The SSO is comprised of four Ritchey–Chrétien 1.0 m-class telescopes installed at ESO Paranal Observatory in the Atacama desert (L. Delrez et al. 2018). Designed to hunt for small habitable-zone planets orbiting ultra-cool stars (M. Gillon 2018; D. Sebastian et al. 2021), three out of four telescopes are equipped with a deep-depletion Andor CCD camera with 2048 × 2048 13.5-μm pixels. Each telescope has a field of view of 12 arcmin × 12 arcmin and a pixel scale of 0.35 arcsec (A. Burdanov et al. 2018; S. Zúñiga-Fernández et al. 2024). Since mid-2022, the fourth telescope of SSO has been equipped with SPIRIT (SPeculoos' Infra-Red photometric Imager for Transits) (see e.g. C. Janó Muñoz et al. 2025), which is an InGaAs CMOS-based instrument, with a custom wide-pass filter called *zYJ* (P. P. Pedersen et al. 2024), designed to be optimized for observing SPECULOOS' cooler targets and to minimize the effects of precipitable water vapour (P. P. Pedersen et al. 2023). This instrument has a smaller field of view of 6.7 arcmin × 5.3 arcmin given its detector size of 1280 × 1024 at 12-μm pitch.

All SPECULOOS observations are processed in the first instance by an automatic data reduction pipeline, presented in C. A. Murray et al. (2020). Successful observations of non-survey targets are then reprocessed using PROSE, a publicly available PYTHON framework for processing astronomical images[8] as described in L. J. Garcia et al. (2021, 2022). Images are calibrated and aligned before performing aperture photometry on the 500 brightest sources detected; PROSE then performs differential photometry (C. Broeg, M. Fernández & R. Neuhäuser 2005) on the target star to extract the light curve.

For TOI-6716 b, we observed one full transit with SSO/Europa on 2025 April 3 in the *Sloan-r'* band with an exposure time of 26 s. For TOI-7384 b, we observed 11 full transits. The first observations were observed simultaneously with SSO/Callisto (in $I + z$') and SSO-Ganymede (in *Sloan-g'*) on 2021 October 14, with exposure times of 17 and 120 s, respectively. We then observed again simultaneously on 2022 Octobet 23 with SSO/Io in the $I + z$' band, and SSO/Callisto in the *zYJ* band, with exposure times of 17 and 20 s, respectively. Our third simultaneous observation of a full TOI-7384 b transit was on 2022 November 17, with SSO/Io (in *Sloan-g'*, exposure time of 120 s), SSO/Europa (in *Sloan-z'*, exposure time of 26 s), and SSO/Callisto (in *zYJ*, exposure time of 20 s). The final four transits were obtained on 2022 December 12 with SS0/Io (in $I + z'$, with an exposure time of 17 s) and three simultaneous observations on 2023 January 6 with SSO/Ganymede (in $Sloan - i'$, with an exposure time of 36 s), SSO/Io (in $I + z'$, with an exposure time of 17 s), and SSO/Europa (in $Sloan - r'$, with an exposure time of 72 s).

6.4.2 TRAPPIST-South

We observed two full transits and one partial transit of TOI-7384 b with TRAPPIST-South (TS) (M. Gillon et al. 2011; E. Jehin et al. 2011), located in ESO La Silla Observatory in Chile. This 0.6-m telescope is equipped with a FLI ProLine PL3041-BB camera and a back-illuminated CCD with a pixel size of 0.64 arcsec, providing a total field of view of 22 arcmin × 22 arcmin for an array of 2048 × 2048 pixels. TS is an f/8 Ritchey–Chrétien telescope on a German equatorial mount.

The full-transit observations took place on UT 2021 September 19 and 2022 April 13, and the partial on 2022 October 26, with an exposure time of 120 s. All transits were observed with the custom $I + z'$ filter to maximize the photometric precision. We reduced the images using PROSE pipeline (L. J. Garcia et al. 2021, 2022) to extract optimal light curves.

6.4.3 LCO-CTIO-1m0

A full transit of TOI-6716 b was observed with the Las Cumbres Observatory Global Telescope (LCOGT; T. M. Brown et al. 2013) 1.0-m network at Cerro Tololo Inter-American Observatory (CTIO). The telescope is equipped with a 4096 × 4096 SINISTRO detector, with an image scale of 0.389 arcsec per pixel and a FOV of 26 arcmin × 26 arcmin. The observation was conducted on 2023 October 28 UT in the Sloan-i' filter with an exposure time of 49 s. The image calibration was performed using the standard LCOGT BANZAI pipeline (C. McCully et al. 2018). The closest

[8] https://github.com/lgrcia/prose.

Gaia star is TIC 777 580 018 at 18.24 arcsec with a $T_{\rm mag}$ of 16.23. We performed the aperture photometry in an uncontaminated aperture of 3.5 arcsec using `AstroImageJ` (K. A. Collins et al. 2017).

6.4.4 *LCOGT-2m0*

Two full transits of TOI-6716 b were observed with LCOGT-2m0 Faulkes Telescope North (FTN) at Haleakala Observatory in Hawaii (HAL) and the LCOGT-2m0 Faulkes Telescope South (FTS) at Siding Spring Observatory in Australia (SSO). The FTN telescope is equipped with the MuSCAT3 multiband imager, while the FTS telescope is equipped with the MuSCAT4 multiband imager (N. Narita et al. 2020). The first transit was observed with MuSCAT4 on UT 2023 October 28, while the second transit was observed with MuSCAT3 on UT 2024 February 4. The observations were conducted simultaneously in the Sloan-g', -r', -i', and Pan-STARRS-z_s filters, with exposure times of 180, 38, 16, and 14 s, respectively. The data processing was performed using the standard LCOGT `BANZAI` pipeline (C. McCully et al. 2018). We performed the aperture photometry using uncontaminated apertures of 4.6–4.8″using `AstroImageJ`.

6.5 Statistical validation

We make use of the statistical validation package TRICERATOPS (S. Giacalone & C. D. Dressing 2020; S. Giacalone et al. 2021) to validate the planetary nature of both candidates. This follows the same procedures outlined in e.g. G. Dransfield et al. (2023), M. L. Silverstein et al. (2024), K. Hesse et al. (2025), M. G. Scott et al. (2025), and L. Thomas et al. (2025); however, we outline this process again here for clarity.

TRICERATOPS evaluates the likelihood that TOI-6716 b and TOI-7384 b are in fact true planets orbiting the target stars. TRICERATOPS also estimates the contributed flux from any nearby stars in order to determine whether one could be the actual source of the observed transit signal. Following this, it fits light-curve models to the phase-folded photometric data in order to calculate relative probabilities for various scenarios, such as transiting planet (TP) and eclipsing binary (EB) on both the target star and nearby stars. TRICERATOPS then calculates a false positive probability (FPP) with a threshold for statistical validation at ≤ 0.015.

For TOI-6716 b we use the two z_s-band light curves from MUSCAT3 and MUSCAT4, and for TOI-7384 b we use the three $I + z'$-band light curves from SSO/Io. We find FPP$< 10^{-8}$, NFPP$< 10^{-7}$ and FPP$< 10^{-14}$, NFPP$< 10^{-17}$ for TOI-6716 b and TOI-7384 b, respectively.

7 GLOBAL PHOTOMETRIC ANALYSIS

We use ALLESFITTER (M. N. Günther & T. Daylan 2019, 2021) to jointly model the full photometric data sets described in Section 6.4 (as well as the available *TESS* data) of each planet. ALLESFITTER is a flexible inference package for exoplanet modelling written in PYTHON. It uses ELLC (P. F. L. Maxted 2016) to generate light-curve models and CELERITE (D. Foreman-Mackey et al. 2017) to create Gaussian Process (GP) models. ALLESFITTER then uses either a nested sampling (with DYNESTY J. S. Speagle 2020) or MCMC (with EMCEE D. Foreman-Mackey et al. 2013) algorithm to select the best fitting model. As it is important to be able to quantify why a specific model is favoured over another (for example, a circular versus eccentric model), we choose to use the nested sampling algorithm for this work as at each step in the sampling it calculates the Bayesian evidence from the Bayes factor (R. E. Kass & A. E. Raftery 1995), allowing us to compare the evidence and determine the most statistically favoured model. This section follows process used in similar works (see e.g. G. Dransfield et al. 2023; M. G. Scott et al. 2025); however, we outline the steps again here for clarity.

We adopt the transit parameters from Section 5 as uniform priors, and the stellar parameters described in Section 4 (and displayed in Table 1) as normal priors. The fitted parameters are $R_p/R_\star$, $(R_p + R_\star)/a$, $\cos i$, T_0, and P. Additionally, we make use of PYLDTK (H. Parviainen & S. Aigrain 2015) and Phoenix stellar atmosphere models (T. O. Husser et al. 2013) to calculate quadratic limb darkening coefficients. We reparameterize them following D. M. Kipping (2013) and adopt them as normal priors in our fit. For observations taken in the same photometric band, the limb darkening coefficients are coupled. All prior distributions can be found in Table D1.

We fit for two models (circular and free eccentricity) using the nested sampling algorithm. As in A. H. M. J. Triaud et al. (2011), the eccentricity is parameterized as $\sqrt{e_b}\cos\omega_b$ and $\sqrt{e_b}\sin\omega_b$. We calculate the difference in the log marginal likelihoods (Bayes factor), $\Delta \log Z$, in order to determine which model is favoured. Here, we adopt the circular fit as the null hypothesis, H_0, and the eccentric fit as the alternate hypothesis, H_1. H_1 is preferred over H_0 if $\Delta \log Z > 3$, and strongly preferred if $\Delta \log Z > 5$ (R. Trotta 2008). We find that for TOI-6716 b, there is no strong preference for either model, with $\Delta \log Z = -0.4$, and similarly for TOI-7384 b, with $\Delta \log Z = -1.5$. However, since eccentricity cannot be well constrained from photometry alone, we do not assume that the orbits of these planets are perfectly circular, and thus adopt the eccentric model fit parameters where we place an upper limit (95 per cent confidence) on the eccentricities of both planets to be $e \leq 0.88$ and $e \leq 0.40$ for TOI-6716 b and TOI-7384 b, respectively. We note that our derived results have no significant change between circular and eccentric fits.

In Figs 9 and 10 we present the transits obtained for TOI-6716 b and TOI-7348 b, respectively. Where multiple transits were observed with the same instrument and filter, the transits are presented phase-folded. All fitted and derived parameters are presented in Tables 4 and 5.

As an additional validation check, we perform the fit again using the priors in Table D1; however, we allow free dilution ($\mathcal{U}[-1, 1]$) in order to check for chromaticity. Dilution is coupled between observations taken in the same band. ALLESFITTER provides the fitted diluted minimum in-transit flux from each instrument, which we then correct with the calculated impact parameter and respective limb darkening coefficients to obtain $R_{\rm p}/R_\star$ in each band. If TOI-6716 b and TOI-7384 b are, in fact, planets (rather than, e.g. eclipsing binaries), we would expect consistent depths across the photometric bands they were observed in, i.e. achromaticity. In Fig. 11, we present these averaged depths for both targets transits, and show that all depths are consistent to 1σ.

Finally, we also compare the stellar host densities calculated by ALLESFITTER from the transit parameters (following S. Seager & G. Mallén-Ornelas 2003) to that of the stellar density priors calculated from the SED parameters for each star. For both TOI-6716 and TOI-7384, we find these values to be within 1σ of the stellar density priors (25.44 ± 5.11 and 13.78 ± 2.43, respectively),

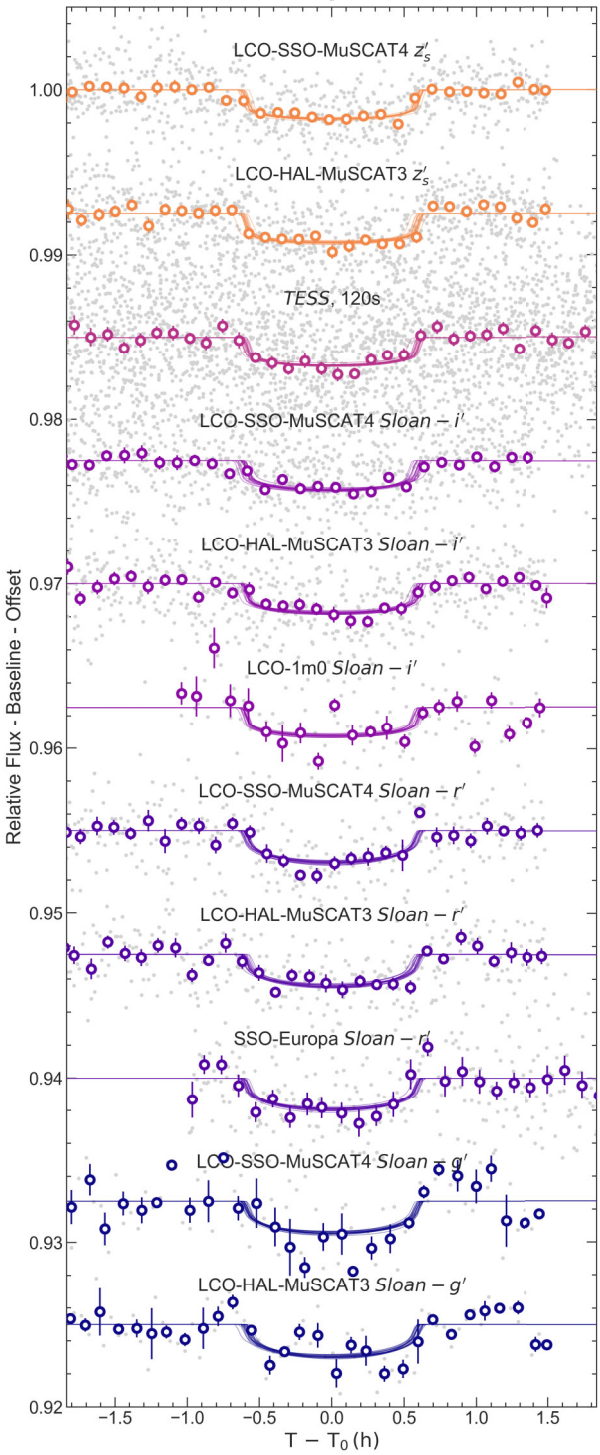

Figure 9. Phase-folded transits of TOI-6716 b from *TESS* 2-min cadence and follow-up ground-based observations. Raw flux points are shown in grey and binned (8 min) in white circles. Transit models are corrected by subtracting the baseline, and all have a relative offset applied for plotting purposes. Model lines comprise of 20 random draws from the posterior transit model.

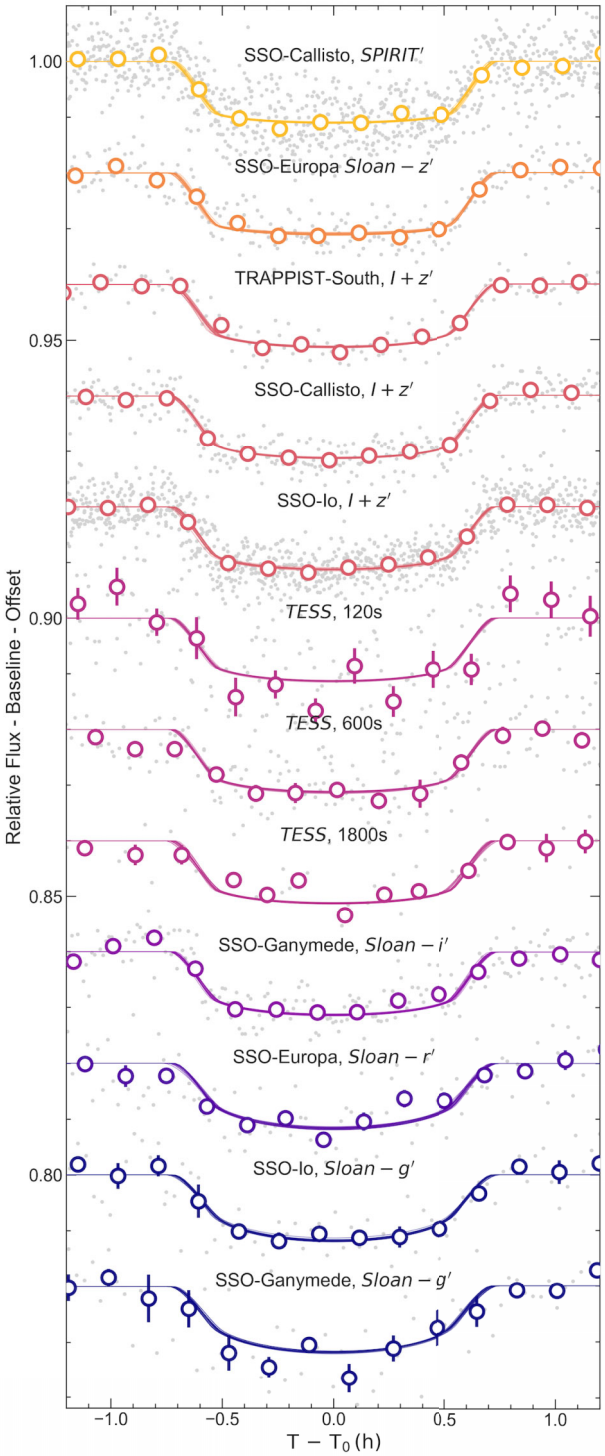

Figure 10. Phase-folded transits of TOI-7384 b from *TESS* 2-,10-, and 30-min cadence and follow-up ground-based observations. Raw flux points are shown in grey and binned (10 min) in white circles. Transit models are corrected by subtracting the baseline, and all have a relative offset applied for plotting purposes. Model lines comprise of 20 random draws from the posterior transit model.

Table 4. Fitted parameters from achromatic eccentric fits for TOI-6716 b. and TOI-7384 b.

Parameter	6716 b	7384 b
	Fitted parameters	
$R_b/R_\star$	$0.03898^{+0.00081}_{-0.00075}$	0.10238 ± 0.00082
$(R_\star + R_b)/a_b$	$0.0348^{+0.0027}_{-0.0023}$	$0.0371^{+0.0023}_{-0.0018}$
$\cos i_b$	$0.0096^{+0.0072}_{-0.0062}$	$0.0211^{+0.0032}_{-0.0023}$
$T_{0;b}$ (BJD)	$2459632.34484^{+0.00062}_{-0.00086}$	$2459565.10114^{+0.00018}_{-0.00017}$
P_b (d)	$4.7185898^{+0.0000054}_{-0.0000041}$	$6.2340258^{+0.0000034}_{-0.0000036}$
$\sqrt{e_b}\cos\omega_b$	$-0.04^{+0.48}_{-0.62}$	$0.03^{+0.39}_{-0.37}$
$\sqrt{e_b}\sin\omega_b$	-0.16 ± 0.23	$-0.00^{+0.18}_{-0.16}$
$q_{1;\mathrm{TESS}}$	$0.302^{+0.046}_{-0.043}$	0.2853 ± 0.0045
$q_{2;\mathrm{TESS}}$	$0.309^{+0.040}_{-0.042}$	0.3044 ± 0.0049
$q_{1;\mathrm{i'}}$	$0.395^{+0.041}_{-0.043}$	0.3431 ± 0.0047
$q_{2;\mathrm{i'}}$	$0.294^{+0.039}_{-0.043}$	0.3083 ± 0.0046
$q_{1;\mathrm{g'}}$	$0.760^{+0.048}_{-0.043}$	0.6875 ± 0.0044
$q_{2;\mathrm{g'}}$	0.323 ± 0.046	0.3585 ± 0.0047
$q_{1;\mathrm{r'}}$	0.685 ± 0.042	0.5983 ± 0.0044
$q_{2;\mathrm{r'}}$	0.361 ± 0.040	0.3772 ± 0.0045
$q_{1;\mathrm{z_s}}$	0.270 ± 0.042	-
$q_{2;\mathrm{z_s}}$	0.261 ± 0.039	-
$q_{1;\mathrm{I+z'}}$	–	0.2644 ± 0.0046
$q_{2;\mathrm{I+z'}}$	–	0.2884 ± 0.0045
$q_{1;\mathrm{z'}}$	–	0.1288 ± 0.0045
$q_{2;\mathrm{z'}}$	–	0.2881 ± 0.0046
$q_{1;\mathrm{spirit}}$	–	0.1338 ± 0.0044
$q_{2;\mathrm{spirit}}$	–	0.2874 ± 0.0044
$\ln\sigma_{\mathrm{TESS}_{120s}}$	-5.5237 ± 0.0068	-4.300 ± 0.018
$\ln\sigma_{\mathrm{TESS}_{600}}$	–	-5.408 ± 0.026
$\ln\sigma_{\mathrm{TESS}_{1800}}$	–	-5.850 ± 0.050
$\ln\sigma_{\mathrm{LCO1m0}_{\mathrm{i'}}}$	$-6.205^{+0.068}_{-0.058}$	-
$\ln\sigma_{\mathrm{LCO-SSO-M4}_{\mathrm{i'}}}$	-6.492 ± 0.027	-
$\ln\sigma_{\mathrm{LCO-Hal-M3}_{\mathrm{i'}}}$	$-6.377^{+0.032}_{-0.030}$	-
$\ln\sigma_{\mathrm{ganymede}_{\mathrm{i'}}}$	–	$-5.735^{+0.025}_{-0.026}$
$\ln\sigma_{\mathrm{LCO-SSO-M4}_{\mathrm{g'}}}$	-6.281 ± 0.083	-
$\ln\sigma_{\mathrm{LCO-Hal-M3}_{\mathrm{g'}}}$	$-6.669^{+0.087}_{-0.072}$	-
$\ln\sigma_{\mathrm{ganymede}_{\mathrm{g'}}}$	–	$-5.094^{+0.053}_{-0.049}$
$\ln\sigma_{\mathrm{io}_{\mathrm{g'}}}$	–	$-5.562^{+0.053}_{-0.049}$
$\ln\sigma_{\mathrm{europa}_{\mathrm{r'}}}$	-5.948 ± 0.039	-5.337 ± 0.035
$\ln\sigma_{\mathrm{LCO-SSO-M4}_{\mathrm{r'}}}$	$-6.433^{+0.042}_{-0.037}$	-
$\ln\sigma_{\mathrm{LCO-Hal-M3}_{\mathrm{r'}}}$	$-6.488^{+0.039}_{-0.037}$	-
$\ln\sigma_{\mathrm{LCO-SSO-M4}_{\mathrm{z_s}}}$	$-6.544^{+0.026}_{-0.021}$	-
$\ln\sigma_{\mathrm{LCO-Hal-M3}_{\mathrm{z_s}}}$	-6.434 ± 0.024	-
$\ln\sigma_{\mathrm{Io}_{\mathrm{I+z'}}}$	–	-5.712 ± 0.013
$\ln\sigma_{\mathrm{TRAPPIST\,SOUTH}_{\mathrm{I+z'}}}$	–	$-5.869^{+0.051}_{-0.048}$
$\ln\sigma_{\mathrm{callisto}_{\mathrm{I+z'}}}$	–	-5.855 ± 0.024
$\ln\sigma_{\mathrm{europa}_{\mathrm{z'}}}$	–	-5.982 ± 0.029
$\ln\sigma_{\mathrm{spirit}}$	–	-5.370 ± 0.014

suggesting the planetary transit signal is produced over the target star.

8 DISCUSSION AND CONCLUSION

TOI-6716 and TOI-7384 join the select club of mid-type fully convective M-dwarfs known to host temperate planets. TOI-6716 b is an Earth-sized, $R_\mathrm{b} = 0.98 \pm 0.07\,\mathrm{R}_\oplus$, exoplanet orbiting with a period of $P = 4.7185898^{+0.0000054}_{-0.0000041}$ d, thus receiving an instellation flux of $S_\mathrm{b} = 4.4 \pm 1.1\,\mathrm{S}_\oplus$. This places it near the inner edge of the temperate zone. TOI-7384 b is a Neptune-sized exoplanet, with $R_\mathrm{b} = 3.56 \pm 0.21\,\mathrm{R}_\oplus$, that orbits with a period of $P = 6.2340258^{+0.0000034}_{-0.0000036}$ d and receives a similar instellation flux of $S_\mathrm{b} = 4.9 \pm 1.1\,\mathrm{S}_\oplus$. While neither of these planets fall even within the *optimistic* HZs of their stars (orbital periods between 9.9–43.1 and 14.4–62.5 d for TOI-6716 and TOI-7384, respectively; R. K. Kopparapu et al. 2013), these planets populate an otherwise sparse region of temperate planet parameter space, offering opportunities for future studies as definitions of exoplanet habitability broaden.

In this section we describe TOI-6176 b and TOI-7384 b within the current population of exoplanets, and then describe briefly the future prospects for follow-up studies.

8.1 TOI-6716 b and TOI-7384 b within the current population

8.1.1 Stellar mass and instellation flux

Fig. 12 shows TOI-6716 b and TOI-7384 b within the current population of exoplanets obtained from the NASA Exoplanet Archive's Composite Database[9], for transiting planets with $0.4 < R_\mathrm{p} < 4\,\mathrm{R}_\oplus$ and $M_\mathrm{p} < 500\,\mathrm{M}_\oplus$. For consistency, we recalculate all planetary instellation fluxes.

The green box highlights planets that fall within the temperate regime, where we see that TOI-6716 b and TOI-7384 b are at the inner (hotter) edge. We also highlight those planets that had SPECULOOS observations that aided in their validation/confirmation, for which the planets in this work also add to this sample.

8.2 Future prospects

8.2.1 More precise planetary radii?

The goal of the TEMPOS programme is to achieve very precise temperate exoplanet radii, ideally ≤ 3 per cent (see Section 3). Currently, TOI-6716 b and TOI-7384 b have radii precisions of 6.8 per cent and 5.9 per cent, respectively, both of which are dominated by their stellar radius precisions (which set planet radius error floors at 6.5 per cent and 5.7 per cent). Thus, in order to significantly improve the planet radius error the stellar radius error must decrease. Surveys such as the EBLM (Eclipsing Binaries-Low Mass) project (A. H. M. J. Triaud et al. 2013b; A. Boetticher et al. 2019; P. F. L. Maxted, A. H. M. J. Triaud & D. V. Martin 2023; M. I. Swayne et al. 2024) are aiming to create an empirical mass–radius–metallicity–luminosity relation using single-lined eclipsing binaries and recently some double-lined systems (D. Sebas-

[9]Retrieved on 2025 July 15, https://exoplanetarchive.ipac.caltech.edu/cgi-bin/TblView/nph-tblView?app=ExoTbls&config = PSCompPars.

Table 5. Derived parameters from achromatic eccentric fit for TOI-6716 b and TOI-7384 b. Since eccentricity is unconstrained, we quote here the 95 per cent confidence upper limit. We thus do not report ω as it was also unconstrained.

Parameter	6716 b	7384 b
Derived parameters		
Host radius over semimajor axis b; $R_\star/a_\mathrm{b}$	$0.0335^{+0.0027}_{-0.0022}$	$0.0337^{+0.0021}_{-0.0017}$
Semimajor axis b over host radius; $a_\mathrm{b}/R_\star$	29.9 ± 2.2	$29.7^{+1.6}_{-1.8}$
Companion radius b over semimajor axis b; $R_\mathrm{b}/a_\mathrm{b}$	$0.001304^{+0.00011}_{-0.000087}$	$0.00345^{+0.00022}_{-0.00018}$
Companion radius b; R_b ($\mathrm{R}_\oplus$)	0.982 ± 0.067	3.56 ± 0.21
Companion radius b; R_b (R_jup)	0.0876 ± 0.0060	0.318 ± 0.018
Semimajor axis b; a_b ($\mathrm{R}_\odot$)	6.87 ± 0.67	9.45 ± 0.78
Semimajor axis b; a_b (AU)	0.0319 ± 0.0031	0.0439 ± 0.0036
Inclination b; i_b (deg)	$89.45^{+0.36}_{-0.42}$	$88.79^{+0.13}_{-0.18}$
Eccentricity b; e_b	≤ 0.88	≤ 0.40
Impact parameter b; $b_\mathrm{tra;b}$	0.27 ± 0.17	$0.611^{+0.031}_{-0.037}$
Total transit duration b; $T_\mathrm{tot;b}$ (h)	1.237 ± 0.015	1.452 ± 0.015
Full-transit duration b; $T_\mathrm{full;b}$ (h)	$1.135^{+0.014}_{-0.016}$	1.041 ± 0.018
Host density from orbit b; $\rho_{\star;\mathrm{b}}$ (cgs)	$22.6^{+5.1}_{-4.6}$	12.8 ± 2.2
Equilibrium temperature b; $T_\mathrm{eq;b}$ (K)	369^{+17}_{-16}	378^{+15}_{-13}
Instellation Flux b; S_b ($\mathrm{S}_\oplus$)	$S_\mathrm{b} = 4.4 \pm 1.1\,\mathrm{S}_\oplus$	$S_\mathrm{b} = 4.9 \pm 1.1\,\mathrm{S}_\oplus$
Limb darkening; $u_{1;\mathrm{TESS}}$	0.338 ± 0.059	0.3251 ± 0.0058
Limb darkening; $u_{2;\mathrm{TESS}}$	0.210 ± 0.044	0.2089 ± 0.0055
Limb darkening; $u_{1;\mathrm{i'}}$	$0.368^{+0.052}_{-0.058}$	0.3611 ± 0.0064
Limb darkening; $u_{2;\mathrm{i'}}$	$0.258^{+0.057}_{-0.051}$	0.2246 ± 0.0054
Limb darkening; $u_{1;\mathrm{g'}}$	0.564 ± 0.081	$0.5944^{+0.0082}_{-0.0076}$
Limb darkening; $u_{2;\mathrm{g'}}$	0.310 ± 0.083	0.2346 ± 0.0077
Limb darkening; $u_{1;\mathrm{r'}}$	0.597 ± 0.073	0.5834 ± 0.0071
Limb darkening; $u_{2;\mathrm{r'}}$	0.230 ± 0.067	0.1899 ± 0.0072
Limb darkening; $u_{1;\mathrm{z_s}}$	$0.269^{+0.053}_{-0.048}$	-
Limb darkening; $u_{2;\mathrm{z_s}}$	$0.246^{+0.045}_{-0.042}$	-
Limb darkening; $u_{1;\mathrm{I+z'}}$	–	0.2966 ± 0.0055
Limb darkening; $u_{2;\mathrm{I+z'}}$	–	0.2176 ± 0.0050
Limb darkening; $u_{1;\mathrm{z'}}$	–	$0.2069^{+0.0046}_{-0.0050}$
Limb darkening; $u_{2;\mathrm{z'}}$	–	0.1521 ± 0.0044
Limb darkening; $u_{1;\mathrm{spirit}}$	–	0.2103 ± 0.0049
Limb darkening; $u_{2;\mathrm{spirit}}$	–	0.1554 ± 0.0042
Combined host density from all orbits; $\rho_{\star;\mathrm{combined}}$ (cgs)	$22.6^{+5.1}_{-4.6}$	12.8 ± 2.2

tian et al. 2024; T. A. Baycroft et al. 2025; D. Sebastian et al. 2025; A. H. M. J. Triaud et al. 2025). An new analysis of the project's result recently achieved a radius accuracy of 1.4 per cent (Davis et al., in preparation) across dozens of systems. When these binary star results will have been used to derive new mass/radius relations, we expect to achieve accurate and precise masses and radii for low-mass field M dwarfs, which when included into the TEMPOS program will aid in reaching our planetary radius precision goal (≤ 3 per cent). For TOI-6716 b, we estimate that in order to reach a planet radius precision of ≤ 3 per cent with a reasonable number of additional observations (e.g. 10), we require that the stellar radius precision increase to 2.32 per cent (assuming a precision of 450 ppm on the transit depth for a single transit with SPECULOOS). Similarly for TOI-7384 b, we require that the stellar radius precision increase to 2.9 per cent, assuming a precision of 500 ppm on the transit depth for a single transit with SPECULOOS.

8.2.2 Planetary mass and atmospheric prospects

In order to fully characterize a planet it is crucial to obtain its density, something that requires both photometric and spectroscopic observations. For small Earth-sized planets, however, obtaining precise radial velocities often proves challenging, especially around late-type M dwarfs given the stellar contamination (see e.g. D. A. Turner et al. 2025). Using the mass–radius relations from J. Chen & D. Kipping (2017), we predict the masses of TOI-6716 b and TOI-7384 b to be $0.9 \pm 0.23\,\mathrm{M}_\oplus$ and $12.4 \pm 1.2\,\mathrm{M}_\oplus$, leading to predicted radial velocity semi-amplitudes[10] of 0.9 ± 0.25 and $9.0 \pm 1.2\,\mathrm{m\,s^{-1}}$, respectively.

[10] calculated from $K = \left(\frac{2\pi G}{P}\right)^{1/3} \frac{M_\mathrm{P} \sin(i)}{M_\star^{2/3}}$, where M_P, $M_\star$ are the planet and star masses, P is the orbital period, i is the inclination, and G is the gravitational constant.

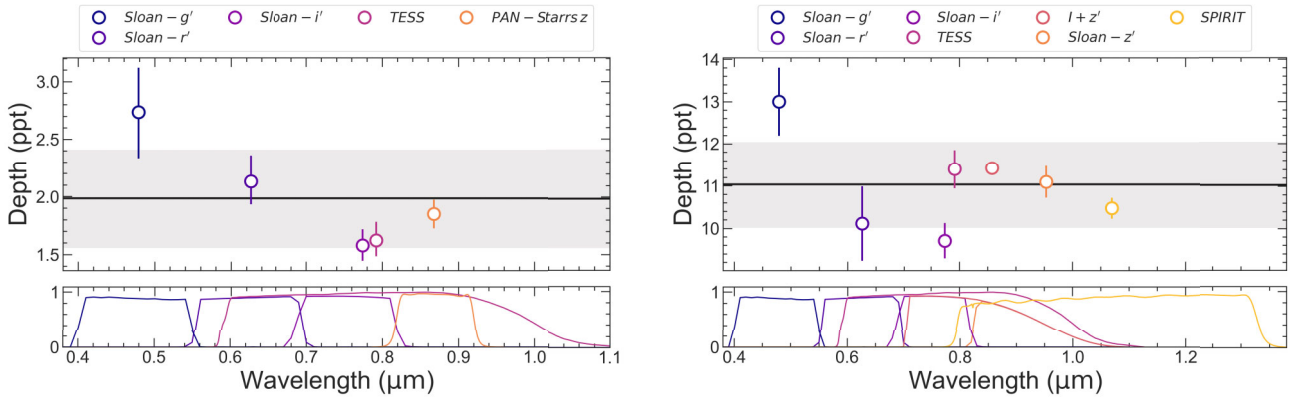

(a) TOI-6716 b averaged depths with dilution from chromatic fit.

(b) TOI-7384 b averaged depths with dilution from chromatic fit.

Figure 11. Chromaticity check of TOI-6716 b (left) and TOI-7384 b (right). Depths are obtained from the chromatic fit and are corrected for limb-darkening. The grey band shows the mean depth and coloured points show the average depths in each band. For TOI-6716 b, all bands agree to within 1.3σ. For TOI-7384 b, all bands agree to within 1.6σ.

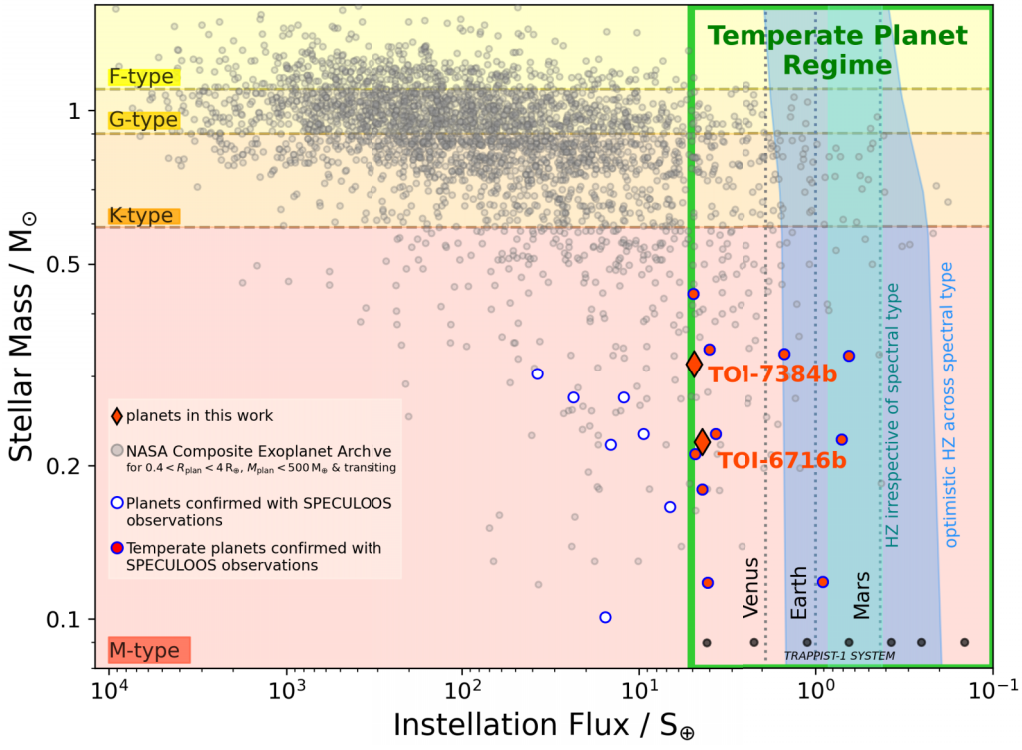

Figure 12. Stellar mass versus instellation flux for transiting planets with $0.4 < R_p < 4\,R_\oplus$ and $M_p < 500\,M_\oplus$ obtained from the Composite NASA exoplanet archive (small, grey points). Instellation flux recalculated for all planets for consistency. Approximate spectral types are indicated by the shaded background and highlighted labels. Planets for which SPECULOOS observations contributed to the validation/confirmation are highlighted with blue circles. TOI-6716 b and TOI-7384 b are depicted by red diamonds, and sit at the inner (hotter) edge of the temperate regime (shown by the green box).

From the MAROON-X exposure time calculator (A. Seifahrt et al. 2018), we could achieve an RV precision of $1.8\,m\,s^{-1}$ per measurement with an exposure time of 1800 s at an SNR$\sim$ 120 for TOI-6716. Therefore, for a 5σ measurement on the mass (i.e. $\sim$ 20 per cent precision) of TOI-6716 b, $\sim$ 200 spectra would need to be collected, where we assume that only approximately two-thirds measurements truly contributed to the mass measurement. For TOI-7384, we find an RV precision of $11.6\,m\,s^{-1}$, and with an expected SNR$\sim$ 23, we would require $\sim$ 100 spectra for a 5σ measurement on the mass of TOI-7384 b. We assume here that both stars rotate relatively slowly, i.e. $v \sin i \lesssim 2\,km\,s^{-1}$, an assumption that can be made for old relatively inactive M dwarfs (C. Moutou et al. 2017; A. Reiners et al. 2022).

We also repeat this calculation for observations with NIRPS (F. Bouchy et al. 2025), where we calculate the expected precision on a singular measurement for an M4 star using

$$\sigma_{RV} = 0.42 \times 10^{(0.94\,H_{mag}-5)/5} \quad (1)$$

(É. Artigau et al. 2024; F. Bouchy et al. 2025). We find precisions of 2.99 and 6.65 m s^{-1} for TOI-6716 and TOI-7384, respectively, for an exposure time of 1800 s. Thus for a 5 σ mass measurement, we would require ∼600 measurements for TOI-6716 b, and ∼30 measurements for TOI-7384 b.

ESPRESSO (F. Pepe et al. 2021) is another high-resolution spectrograph that could obtain RV measurements for our planetary mass measurements. However, from the ESPRESSO ETC, we calculate that for a 5 σ mass measurement, we would require ∼770 and ∼70 measurements of TOI-6716 and TOI-7384, assuming RV precisions of 3.3 and 10 m s^{-1}, respectively, therefore making this facility less favourable compared to NIRPS or MAROON-X for these science goals.

While for TOI-7384 b a fairly reasonable number of measurements are required to make a significant mass measurement (but still difficult to obtain on competitive facilities), this is not the case for small likely Earth-mass planet TOI-6716 b, where a much larger amount of telescope time would be required.

We emphasize that these RV estimates are based on the assumption that the predicted mass is correct; however, this is not always the case and can sometimes be largely overpredicted or underpredicted, which naturally will affect the number of RV measurements required (specifically for the underpredicted case). A recent example of this is TOI-6478 b (M. G. Scott et al. 2025), who calculated that based on the predicted mass of the planet, 10 RVs from MAROON-X would be sufficient to obtain a 3–4σ constraint. However, the planet is seemingly underdense, and as such those 10 RVs could not constrain the mass at all, and only provided an upper mass limit.

Naturally, the next step in understanding these planets could be observations of their atmospheres. E. M. R. Kempton et al. (2018) define a transmission spectroscopy metric (TSM), which is proportional to the SNR expected from the strength of possible transit features. Large TSMs are indicative of strong features, thus facilitating more detailed and accurate atmospheric characterization. For TOI-6716 b we predict TSM ∼ 13 (similar to the outer TRAPPIST-1 planets), and for TOI-7384 b TSM ∼ 69. An ongoing question, however, is whether small rocky planets around M dwarfs can retain their atmospheres; studies into the M dwarf cosmic shoreline aim to inform this debate, allowing for more targeted follow-up with, e.g. *JWST* (see e.g. Q. Xue et al. 2025). E. K. Pass, D. Charbonneau & A. Vanderburg (2025) investigate the cosmic shoreline for late-type M dwarfs, and calculate the cumulative historic X-ray and ultraviolet irradiation received by a planet, I_{XUV}, as a function of stellar mass. Fig. 2 in their work shows $I_{XUV,\oplus}$ versus escape velocity, $v_{\rm esc}$, with regions of atmospheric loss and retention and planets with $R_{\rm p} < 1.8\,{\rm R}_\oplus$.

We calculate $v_{\rm esc} = \sqrt{\frac{M_{\rm P}}{{\rm M}_\oplus}\frac{{\rm R}_\oplus}{R_{\rm P}}}\,v_{{\rm esc},\oplus}$ and find $v_{\rm esc} = 0.96\,v_{{\rm esc},\oplus}$ (= 10.7 km s^{-1}) for TOI-6716 b. We then estimate $I_{\rm XUV} = 422\,I_{{\rm XUV},\oplus}$ using values in table 1[11] from E. K. Pass et al. (2025), placing it within the region of atmospheric loss. E. K. Pass et al. (2025) also define an 'atmospheric retention metric' (ARM), which quantifies the position of the planet relative to the cosmic shoreline, for which we find ARM∼ −1.66. Therefore, we expect that TOI-6716 b is unlikely to have retained its atmosphere; however, this is likely not the case for the more massive TOI-7384 b, making it an ideal target for future *JWST* observations.

[11]We take values for TOI-6716 from the $M_\star = 0.25\,{\rm M}_\odot$ row in table 1 from E. K. Pass et al. (2025).

8.3 Summary

We report the discovery and validation of two temperate planets – an Earth-sized planet, TOI-6716 b, and a Neptune-sized planet, TOI-7384 b – transiting fully convective M dwarfs. These planets add to the small but growing sample of planets in the temperate region that we have defined in this work, $0.1\,{\rm S}_\oplus < S < 5\,{\rm S}_\oplus$.

The planets were initially identified with *TESS* and validated through an extensive campaign of high-resolution imaging, ground-based transit observations with SPECULOOS, TRAPPIST-South, and LCOGT, as well as reconnaissance spectroscopy of the host stars. Statistical analysis with TRICERATOPS yields FPPs of $<10^{-8}$ and $<10^{-14}$ for TOI-6716 b and TOI-7384 b, respectively. Injection–recovery tests show that additional short-period planets larger than $\sim 1\,R_\oplus$ can be excluded for TOI-6716, while Earth-sized companions remain undetectable for the current data on TOI-7384.

Given its small radius and high irradiation, TOI-6716 b may be airless; however, with a predicted TSM similar to that of the outer TRAPPIST-1 planets, should it have an atmosphere it could be a good target for rocky-world atmospheric observations with *JWST*. In terms of TOI-7384 b, its size and predicted mass make it an attractive target for atmospheric characterization with *JWST* and future facilities. Together these discoveries show the power of combining *TESS* with coordinated ground-based efforts to build a catalogue of temperate planets around fully convective M dwarfs for atmospheric studies in the coming decade.

ACKNOWLEDGEMENTS

MGS acknowledges support from the UK Science and Technology Facilities Council (STFC) and from a local studentship delivered by the College of Engineering and Physical Sciences of the University of Birmingham.

The ULiege's contribution to SPECULOOS has received funding from the European Research Council under the European Union's Seventh Framework Programme (FP/2007-2013) (grant Agreement n° 336480/SPECULOOS), from the Balzan Prize and Francqui Foundations, from the Belgian Scientific Research Foundation (F.R.S.-FNRS; grant n° T.0109.20), from the University of Liege, and from the ARC grant for Concerted Research Actions financed by the Wallonia-Brussels Federation. This work is supported by a grant from the Simons Foundation (PI Queloz, grant number 327127). J.d.W. and MIT gratefully acknowledge financial support from the Heising-Simons Foundation, Dr and Mrs Colin Masson and Dr Peter A. Gilman for Artemis, the first telescope of the SPECULOOS network situated in Tenerife, Spain. This work is supported by the Swiss National Science Foundation (PP00P2-163967, PP00P2-190080 and the National Centre for Competence in Research PlanetS). This work has received fund from the European Research Council (ERC) under the European Union's Horizon 2020 research and innovation programme (grant agreement n° 803193/BEBOP), from the MERAC foundation, and from the Science and Technology Facilities Council (STFC; grant n° ST/S00193X/1) and from the ERC/UKRI Frontier Research Guarantee programme (EP/Z000327/1/CandY). TRAPPIST is funded by the Belgian Fund for Scientific Research (Fond National de la Recherche Scientifique, FNRS) under the grant PDR T.0120.21, with the participation of the Swiss National Science Fundation (SNF). Data have been collected from the ESO la Silla Observatory in Chile. SPECULOOS and TRAPPIST also acknowledge support

from the F.R.S.-FNRS (PDR 35292916 and 40028002). MG and EJ are F.R.S.-FNRS Research Directors. A. S postdoctoral fellowship is funded by F.R.S.-FNRS research project ID 40028002 (Detection and Study of Rocky Worlds)

This material is based upon work supported by the National Aeronautics and Space Administration under Agreement No. 80NSSC21K0593 for the program 'Alien Earths'. The results reported herein benefited from collaborations and/or information exchange within NASA's Nexus for Exoplanet System Science (NExSS) research coordination network sponsored by NASA's Science Mission Directorate. This material is based upon work supported by the European Research Council (ERC) Synergy Grant under the European Union's Horizon 2020 research and innovation program (grant No. 101118581 – project REVEAL). Visiting Astronomer at the Infrared Telescope Facility, which is operated by the University of Hawaii under contract 80HQTR24DA010 with the National Aeronautics and Space Administration. Funding for KB was provided by the European Union (ERC AdG SUBSTELLAR, GA 101054354). YGMC was supported by UNAM-PAPIIT-IG101224. FJP acknowledges financial support from the Severo Ochoa grant CEX2021-001131-S funded by MCIN/AEI/10.13039/501100011033 and Ministerio de Ciencia e Innovación through the project PID2022-137241NB-C43. This work makes use of observations from the LCOGT network. Part of the LCOGT telescope time was granted by NOIRLab through the Mid-Scale Innovations Program (MSIP). MSIP is funded by NSF. This research has made use of the Exoplanet Follow-up Observation Program (ExoFOP; DOI: 10.26134/ExoFOP5) website, which is operated by the California Institute of Technology, under contract with the National Aeronautics and Space Administration under the Exoplanet Exploration Program. Funding for the TESS mission is provided by NASA's Science Mission Directorate. KAC acknowledges support from the TESS mission via subaward s3449 from MIT. This work is partly supported by JSPS KAKENHI Grant Numbers JP24H00017, JP24K00689, and JSPS Bilateral Program Number JPJSBP120249910. This paper is based on observations made with the MuSCAT instruments, developed by the Astrobiology Center (ABC) in Japan, the University of Tokyo, and Las Cumbres Observatory (LCOGT). MuSCAT3 was developed with financial support by JSPS KAKENHI (JP18H05439) and JST PRESTO (JPMJPR1775), and is located at the Faulkes Telescope North on Maui, HI (USA), operated by LCOGT. MuSCAT4 was developed with financial support provided by the Heising-Simons Foundation (grant 2022-3611), JST grant number JPMJCR1761, and the ABC in Japan, and is located at the Faulkes Telescope South at Siding Spring Observatory (Australia), operated by LCOGT. The paper is based on observations made with the Kast spectrograph on the Shane 3m telescope at Lick Observatory. A major upgrade of the Kast spectrograph was made possible through generous gifts from the Heising-Simons Foundation and William and Marina Kast. We acknowledge that Lick Observatory sits on the unceded ancestral homelands of the Chochenyo and Tamyen Ohlone peoples, including the Alson and Socostac tribes, who were the original inhabitants of the area that includes Mt. Hamilton. TD acknowledges support from the McDonnell Center for the Space Sciences at Washington University in St. Louis. Some of the observations in this paper made use of the High-Resolution Imaging instrument Zorro and were obtained under Gemini LLP Proposal Number: GN/S-2021A-LP-105. Zorro was funded by the NASA Exoplanet Exploration Program and built at the NASA Ames Research Center by Steve B. Howell, Nic Scott, Elliott P. Horch, and Emmett Quigley. Zorro was mounted on the Gemini South telescope of the international Gemini Observatory, a program of NSF's OIR Lab, which is managed by the Association of Universities for Research in Astronomy (AURA) under a cooperative agreement with the National Science Foundation. on behalf of the Gemini partnership: the National Science Foundation (United States), National Research Council (Canada), Agencia Nacional de Investigación y Desarrollo (Chile), Ministerio de Ciencia, Tecnología e Innovación (Argentina), Ministério da Ciência, Tecnologia, Inovações e Comunicações (Brazil), and Korea Astronomy and Space Science Institute (Republic of Korea). B.-O. D. and YGMC acknowledge support from the Swiss National Science Foundation (IZSTZ0_216537).

DATA AVAILABILITY

TESS data products are available via the MAST portal at https://mast.stsci.edu/portal/Mashup/Clients/Mast/Portal.html Follow-up observations (photometry, high-resolution imaging data) are available on ExoFOP or on request.

REFERENCES

Aller A., Lillo-Box J., Jones D., Miranda L. F., Barceló Forteza S., 2020, A&A, 635, A128
Artigau É. et al., 2024, in Bryant J. J., Motohara K., Vernet J. R. D. eds, Proc. SPIE Conf. Ser. Vol. 13096, Ground-Based and Airborne Instrumentation for Astronomy X. SPIE, Bellingham, p. 130960C
Bailer-Jones C. A. L., Rybizki J., Fouesneau M., Demleitner M., Andrae R., 2021, AJ, 161, 147
Barkaoui K. et al., 2024, A&A, 687, A264
Barkaoui K. et al., 2025, A&A, 695, A281
Baycroft T. A. et al., 2025, MNRAS, 541, 2801
Bochanski J. J., West A. A., Hawley S. L., Covey K. R., 2007, AJ, 133, 531
Bouchy F. et al., 2025, A&A, 700, A10
Broeg C., Fernández M., Neuhäuser R., 2005, Astron. Nachr., 326, 134
Brown T. M. et al., 2013, PASP, 125, 1031
Burdanov A., Delrez L., Gillon M., Jehin E., 2018, in Deeg H. J., Belmonte J. A., eds, Handbook of Exoplanets, SPECULOOS Exoplanet Search and Its Prototype on TRAPPIST. Springer International Publishing AG, New York, p. 130
Burgasser A. J., Splat Development Team, 2017, in Coelho P., Martins L., Griffin E., eds, ASI Conference Series, Vol. 14, The SpeX Prism Library Analysis Toolkit (SPLAT): A Data Curation Model. International Workshop on Spectral Stellar Libraries, p. 7
Cadieux C. et al., 2022, AJ, 164, 96
Charbonneau D., Deming D., 2007, preprint (arXiv:0706.1047)
Chen H., Rogers L. A., 2016, ApJ, 831, 180
Chen J., Kipping D., 2017, ApJ, 834, 17
Ciardi D. R., Beichman C. A., Horch E. P., Howell S. B., 2015, ApJ, 805, 16
Collins K. A., Kielkopf J. F., Stassun K. G., Hessman F. V., 2017, AJ, 153, 77
Cowan N. B. et al., 2015, PASP, 127, 311
Cushing M. C., Vacca W. D., Rayner J. T., 2004, PASP, 116, 362
Cushing M. C., Rayner J. T., Vacca W. D., 2005, ApJ, 623, 1115
Cutri R. M. et al., 2003, VizieR Online Data Catalog, II/246
Cutri R. M. et al., 2021, VizieR Online Data Catalog, II/328
Delrez L. et al., 2018, in Marshall H. K., Spyromilio J. eds, Proc. SPIE Conf. Ser. Vol. 10700, Ground-Based and Airborne Telescopes VII. SPIE, Bellingham, 107001I
Delrez L. et al., 2022, A&A, 667, A59
Demory B. O. et al., 2020, A&A, 642, A49
Dévora-Pajares M., Pozuelos F. J., 2022, in Zenodo Software package. p. 65770831

Dévora-Pajares M., Pozuelos F. J., Thuillier A., Timmermans M., Van Grootel V., Bonidie V., Mota L. C., Suárez J. C., 2024, MNRAS, 532, 4752
Dholakia S. et al., 2024, MNRAS, 531, 1276
Dittmann J. A. et al., 2017, Nature, 544, 333
Douglas S. T. et al., 2014, ApJ, 795, 161
Dransfield G. et al., 2024, MNRAS, 527, 35
Encrenaz T., Coustenis A., Gilli G., Marcq E., Molaverdikhani K., Mugnai L. V., Ollivier M., Tinetti G., 2022, Exp. Astron., 53, 375
Feliz D. L., Plavchan P., Bianco S. N., Jimenez M., Collins K. I., Villarreal Alvarado B., Stassun K. G., 2021, AJ, 161, 247
Foreman-Mackey D., Hogg D. W., Lang D., Goodman J., 2013, PASP, 125, 306
Foreman-Mackey D., Agol E., Ambikasaran S., Angus R., 2017, Astrophysics Source Code Library, record ascl:1709.008
Fukui A., 2025, Res. Notes Am. Astron. Soc., 9, 73
Fulton B. J. et al., 2017, AJ, 154, 109
Furlan E., Howell S. B., 2017, AJ, 154, 66
Furlan E., Howell S. B., 2020, ApJ, 898, 47
Gaia Collaboration, 2022, VizieR Online Data Catalog, I/355
Garcia L. J., Timmermans M., Pozuelos F. J., Ducrot E., Gillon M., Delrez L., Wells R. D., Jehin E., 2021, Astrophysics Source Code Library, record ascl:2111.006
Garcia L. J., Timmermans M., Pozuelos F. J., Ducrot E., Gillon M., Delrez L., Wells R. D., Jehin E., 2022, MNRAS, 509, 4817
Gardner J. P. et al., 2006, Space Sci. Rev., 123, 485
Gardner J. P. et al., 2023, PASP, 135, 068001
Ghachoui M. et al., 2023, A&A, 677, A31
Ghachoui M. et al., 2024, A&A, 690, A263
Giacalone S., Dressing C. D., 2020, Astrophysics Source Code Library, record ascl:2002.004
Giacalone S. et al., 2021, AJ, 161, 24
Gillon M., 2018, Nat. Astron., 2, 344
Gillon M., Jehin E., Magain P., Chantry V., Hutsemékers D., Manfroid J., Queloz D., Udry S., 2011, EPJ Web of Conferences, 11, 06002
Gillon M. et al., 2017, Nature, 542, 456
Gizis J. E., 1997, AJ, 113, 806
Gray R. O., Corbally C. J., Garrison R. F., McFadden M. T., Bubar E. J., McGahee C. E., O'Donoghue A. A., Knox E. R., 2006, AJ, 132, 161
Greklek-McKeon M. et al., 2025, AJ, 169, 292
Günther M. N., Daylan T., 2019, Astrophysics Source Code Library, record ascl:1903.003
Günther M. N., Daylan T., 2021, ApJS, 254, 13
Günther M. N. et al., 2019, Nat. Astron., 3, 1099
Gupta A., Schlichting H. E., 2019, MNRAS, 487, 24
Hamuy M., Walker A. R., Suntzeff N. B., Gigoux P., Heathcote S. R., Phillips M. M., 1992, PASP, 104, 533
Hamuy M., Suntzeff N. B., Heathcote S. R., Walker A. R., Gigoux P., Phillips M. M., 1994, PASP, 106, 566
Hauschildt P. H., Allard F., Baron E., 1999, ApJ, 512, 377
Hesse K. et al., 2025, AJ, 170, 108
Howell S. B., Everett M. E., Sherry W., Horch E., Ciardi D. R., 2011, AJ, 142, 19
Howell S. B., Scott N. J., Matson R. A., Everett M. E., Furlan E., Gnilka C. L., Ciardi D. R., Lester K. V., 2021, Front. Astron. Space Sci., 8, 10
Husser T. O., Wende-von Berg S., Dreizler S., Homeier D., Reiners A., Barman T., Hauschildt P. H., 2013, A&A, 553, A6
Janó Muñoz C. et al., 2025, MNRAS, 541, 630
Jehin E. et al., 2011, The Messenger, 145, 2
Jenkins J. M. et al., 2016, in Chiozzi G., Guzman J. C., eds, Proc. SPIE Conf. Ser. Vol. 9913, Software and Cyberinfrastructure for Astronomy IV. SPIE, Bellingham, p. 99133E
Jordi C. et al., 2010, A&A, 523, A48
Kass R. E., Raftery A. E., 1995, J. Am. Stat. Assoc., 90, 773
Kasting J. F., Whitmire D. P., Reynolds R. T., 1993, Icarus, 101, 108
Kempton E. M. R. et al., 2018, PASP, 130, 114401
Kipping D. M., 2013, MNRAS, 435, 2152
Kopparapu R. K. et al., 2013, ApJ, 765, 131
Kopparapu R. K., Ramirez R. M., SchottelKotte J., Kasting J. F., Domagal-Goldman S., Eymet V., 2014, ApJ, 787, L29
Lépine S., Rich R. M., Shara M. M., 2003, AJ, 125, 1598
Lépine S., Hilton E. J., Mann A. W., Wilde M., Rojas-Ayala B., Cruz K. L., Gaidos E., 2013, AJ, 145, 102
Lindgren S., Heiter U., 2017, A&A, 604, A97
Lobo A. H., Shields A. L., Palubski I. Z., Wolf E., 2023, ApJ, 945, 161
Lopez E. D., Rice K., 2018, MNRAS, 479, 5303
Madhusudhan N., Piette A. A. A., Constantinou S., 2021, ApJ, 918, 1
Mallorquín M. et al., 2023, A&A, 680, A76
Mann A. W., Brewer J. M., Gaidos E., Lépine S., Hilton E. J., 2013, AJ, 145, 52
Mann A. W. et al., 2019, ApJ, 871, 63
Martín E. L., Delfosse X., Basri G., Goldman B., Forveille T., Zapatero Osorio M. R., 1999, AJ, 118, 2466
Matson R. A., Howell S. B., Horch E. P., Everett M. E., 2018, AJ, 156, 31
Maxted P. F. L., 2016, A&A, 591, A111
Maxted P. F. L., Triaud A. H. M. J., Martin D. V., 2023, Universe, 9, 498
McCully C., Volgenau N. H., Harbeck D.-R., Lister T. A., Saunders E. S., Turner M. L., Siiverd R. J., Bowman M., 2018, in Guzman J. C., Ibsen J. eds, Proc. SPIE Conf. Ser. Vol. 10707, Software and Cyberinfrastructure for Astronomy V. SPIE, Bellingham, p. 107070K
Menou K., 2013, ApJ, 774, 51
Miles E. L., Ostberg C., Kane S. R., Clarkson O., Unterborn C. T., Fetherolf T., Way M. J., Welter S. G., 2025, AJ, 170, 29
Miller J. S., Stone R. P. S., 1994, Technical Report 66, The Kast Double Spectrograph. University of California Lick Observatory Technical Reports
Morley C. V., Kreidberg L., Rustamkulov Z., Robinson T., Fortney J. J., 2017, ApJ, 850, 121
Moutou C. et al., 2017, MNRAS, 472, 4563
Murgas F. et al., 2023, A&A, 677, A182
Murray C. A. et al., 2020, MNRAS, 495, 2446
Narita N. et al., 2020, in Evans C. J., Bryant J. J., Motohara K., eds, Proc. SPIE Conf. Ser. Vol. 11447, Ground-Based and Airborne Instrumentation for Astronomy VIII. SPIE, Bellingham, p. 114475K
Owen J. E., Wu Y., 2017, ApJ, 847, 29
Parc L., Bouchy F., Venturini J., Dorn C., Helled R., 2024, A&A, 688, A59
Parviainen H., Aigrain S., 2015, MNRAS, 453, 3821
Pass E. K., Charbonneau D., Vanderburg A., 2025, ApJ, 986, L3
Passegger V. M. et al., 2022, A&A, 658, A194
Pedersen P. P. et al., 2023, MNRAS, 518, 2661
Pedersen P. P. et al., 2024, in Bryant J. J., Motohara K., Vernet J. R. D. eds, Proc. SPIE Conf. Ser. Vol. 13096, Ground-Based and Airborne Instrumentation for Astronomy X. SPIE, Bellingham, p. 130963X
Pepe F. et al., 2021, A&A, 645, A96
Peterson M. S. et al., 2023, Nature, 617, 701
Pickles A. J., 1998, PASP, 110, 863
Piette A. A. A., Madhusudhan N., Mandell A. M., 2022, MNRAS, 511, 2565
Pozuelos F. J. et al., 2020, A&A, 641, A23
Pozuelos F. J. et al., 2023, A&A, 672, A70
Rauer H. et al., 2025, Exp. Astron., 59, 26
Rayner J. T., Toomey D. W., Onaka P. M., Denault A. J., Stahlberger W. E., Vacca W. D., Cushing M. C., Wang S., 2003, PASP, 115, 362
Rayner J. T., Cushing M. C., Vacca W. D., 2009, ApJS, 185, 289
Reid I. N., Hawley S. L., Gizis J. E., 1995, AJ, 110, 1838
Reiners A. et al., 2018, A&A, 609, L5
Reiners A. et al., 2022, A&A, 662, A41
Ricker G. R. et al., 2015, J. Astron. Telesc. Instrum. Syst., 1, 014003
Riddick F. C., Roche P. F., Lucas P. W., 2007, MNRAS, 381, 1067
Rogers L. A., 2015, ApJ, 801, 41
Rojas-Ayala B., Covey K. R., Muirhead P. S., Lloyd J. P., 2012, ApJ, 748, 93
Schanche N. et al., 2022, A&A, 657, A45
Schlegel D. J., Finkbeiner D. P., Davis M., 1998, ApJ, 500, 525
Schulze-Makuch D. et al., 2011, Astrobiology, 11, 1041
Scott M. G. et al., 2025, MNRAS, 540, 1909
Scott N. J. et al., 2021, Front. Astron. Space Sci., 8, 138

Seager S., Mallén-Ornelas G., 2003, ApJ, 585, 1038
Seager S., Petkowski J. J., Günther M. N., Bains W., Mikal-Evans T., Deming D., 2021, Universe, 7, 172
Sebastian D. et al., 2021, A&A, 645, A100
Sebastian D. et al., 2024, MNRAS, 530, 2572
Sebastian D. et al., 2025, MNRAS, 540, 2914
Seifahrt A., Stürmer J., Bean J. L., Schwab C., 2018, in Evans C. J., Simard L., Takami H. eds, Proc. SPIE Conf. Ser. Vol. 10702, Ground-Based and Airborne Instrumentation for Astronomy VII. SPIE, Bellingham, p. 107026DarXiv:1805.09276)
Silverstein M. L. et al., 2024, AJ, 167, 255
Simcoe R. A. et al., 2008, in McLean I. S., Casali M. M., eds, Proc. SPIE Conf. Ser. Vol. 7014, Ground-Based and Airborne Instrumentation for Astronomy II. SPIE, Bellingham, p. 70140U
Speagle J. S., 2020, MNRAS, 493, 3132
Stassun K. G., Torres G., 2016, AJ, 152, 180
Stassun K. G., Torres G., 2021, ApJ, 907, L33
Stassun K. G., Collins K. A., Gaudi B. S., 2017, AJ, 153, 136
Stassun K. G., Corsaro E., Pepper J. A., Gaudi B. S., 2018, AJ, 155, 22
Stassun K. G. et al., 2019, AJ, 158, 138
Stevenson K. B., Bean J. L., Seifahrt A., Gilbert G. J., Line M. R., Désert J.-M., Fortney J. J., 2016, ApJ, 817, 141
Sun L., Gu S., Wang X., Schmitt J. H. M. M., Ioannidis P., Kouwenhoven M. B. N., Dou J., Zhao G., 2025, Nat. Astron., 9, 1184
Swayne M. I. et al., 2024, MNRAS, 528, 5703
The JWST Transiting Exoplanet Community Early Release Science Team, 2023, Nature, 7949, 649
Thomas L. et al., 2025, A&A, 694, A143
Timmermans M. et al., 2024, A&A, 687, A48
Tokovinin A., 2018, PASP, 130, 035002
Triaud A. H. M. J. et al., 2011, A&A, 531, A24
Triaud A. H. M. J. et al., 2013a, preprint (arXiv:1304.7248)
Triaud A. H. M. J. et al., 2013b, A&A, 549, A18
Triaud A. H. M. J. et al., 2024, Nat. Astron., 8, 17
Triaud A. H. M. J. et al., 2025, MNRAS, 544, 2180
Trotta R., 2008, Contemp. Phys., 49, 71
Turner D. A. et al., 2025, MNRAS, 545, staf1703
von Boetticher A. et al., 2019, A&A, 625, A150
Wells R., Poppenhaeger K., Watson C. A., 2019, MNRAS, 487, 1865
Wells R. D. et al., 2021, A&A, 653, A97
West A. A., Hawley S. L., Bochanski J. J., Covey K. R., Reid I. N., Dhital S., Hilton E. J., Masuda M., 2008, AJ, 135, 785
Xue Q. et al., 2025, ApJ 995, L52
Yang J., Hu R., 2024, ApJ, 971, L48
Yang J., Cowan N. B., Abbot D. S., 2013, ApJ, 771, L45
Zacharias N., Finch C. T., Girard T. M., Henden A., Bartlett J. L., Monet D. G., Zacharias M. I., 2013, AJ, 145, 44
Ziegler C., Tokovinin A., Briceño C., Mang J., Law N., Mann A. W., 2020, AJ, 159, 19
Zúñiga-Fernández S. et al., 2024, in Marshall H. K., Spyromilio J., Usuda T. eds, Proc. SPIE Conf. Ser. Vol. 13094, Ground-Based and Airborne Telescopes X. SPIE, Bellingham, p. 1309413 https://doi.org/10.1117/12.3020550
Zúñiga-Fernández S., Burdanov A., Delrez L., Gillon M., Jehin E., 2025, SPECULOOS Exoplanet Search and Its Prototype on TRAPPIST. Springer Nature Switzerland, Cham, p. 1, https://doi.org/10.1007/978-3-319-30648-3_130-3

APPENDIX A: ARCHIVAL IMAGES

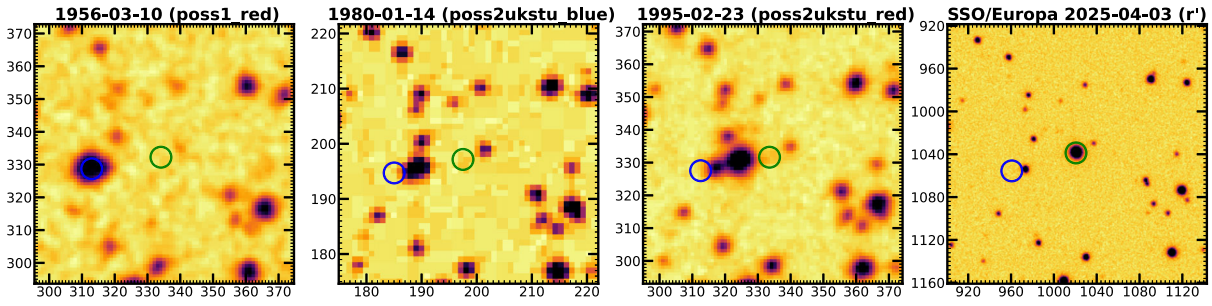

(a) Archival images for TOI-6716.

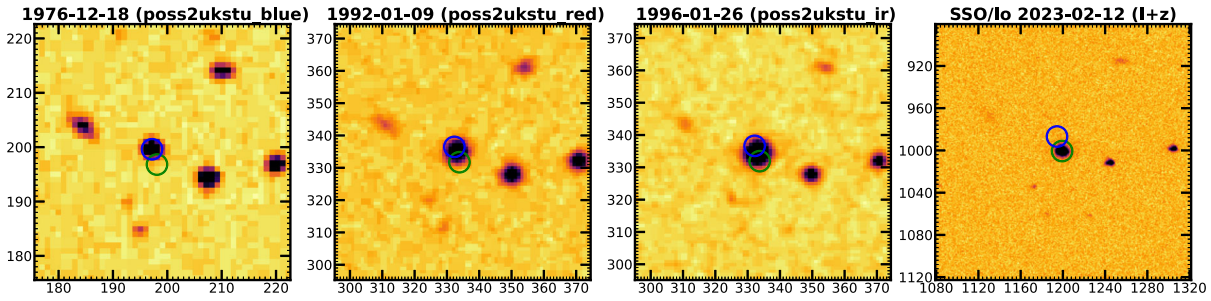

(b) Archival images for TOI-7384.

Figure A1. Archival images for TOI-6716 *(top)* and TOI-7384 (*bottom)*. The blue circles show the position of the star in the earliest image, and the green circles show the position of the star in the most recent images. TOI-6716 has shifted by 22.2 arcsec from 1956 to 2025, and TOI-7384 by 5.2 arcsec from 1976 to 2023. These images show that there is no background star blending with either of our target stars, and thus we conclude the transit event could not have have happened on a blended star.

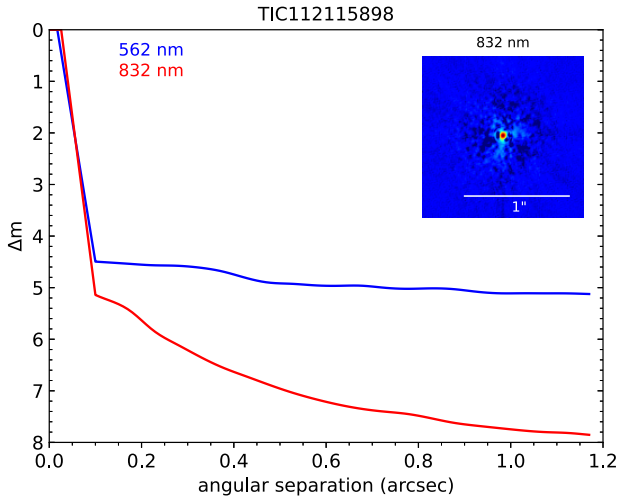

(a) TOI-6716.

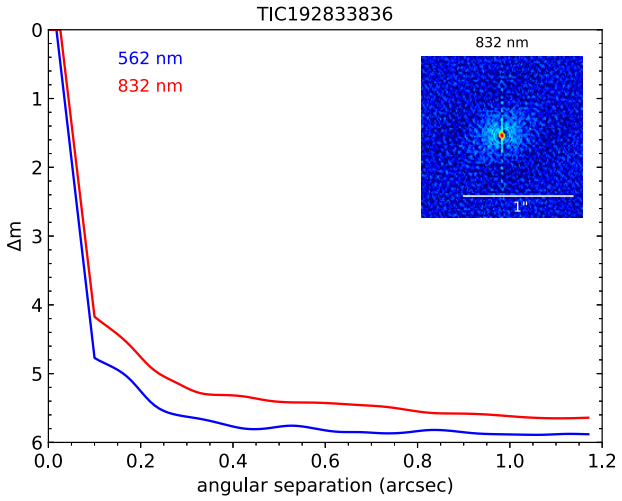

(b) TOI-7384.

Figure B1. The figure shows 5σ magnitude contrast curves in both filters as a function of the angular separation out to 1.2 arcsec. The inset shows the reconstructed 832 nm image of TOI-6716 *(left)* and TOI-7384 *(right)* with a 1 arcsec scale bar. Both stars were found to have no close companions from the diffraction limit (0.02 arcsec) out to 1.2 arcsec to within the magnitude contrast levels achieved.

APPENDIX B: HIGH-RESOLUTION IMAGES–ZORRO

APPENDIX C: HIGH-RESOLUTION IMAGES–SOAR

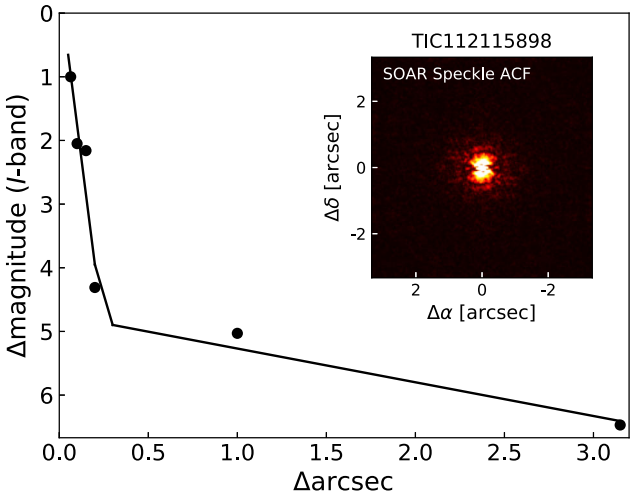

Figure C1. The 5 σ detection sensitivity to nearby companions for the SOAR speckle observation of TOI-6716 as a function of separation from the target star and magnitude difference with respect to the target. Inset is the speckle autocorrelation function from the observation.

APPENDIX D: PRIORS FOR GLOBAL PHOTOMETRIC ANALYSIS

Table D1. Priors used in achromatic eccentric fit for TOI-6716 b and TOI-7384 b.

Parameter	Fit parametrization	
	6716 b	*7384 b*
$R_b/R_\star$	$\mathcal{U}(0.005, 0.05)$	$\mathcal{U}(0.05, 0.15)$
$(R_\star + R_b)/a_b$	$\mathcal{U}(0.02, 0.06)$	$\mathcal{U}(0.03, 0.05)$
$\cos i_b$	$\mathcal{U}(0.0, 0.05)$	$\mathcal{U}(0.0, 0.1)$
$T_{0;b}$ (BJD)	$\mathcal{U}(2458495.1, 2458495.21)$	$\mathcal{U}(2459683.5, 2459683.6)$
P_b (d)	$\mathcal{U}(4.71, 4.72)$	$\mathcal{U}(6.23, 6.24)$
$\sqrt{e_b}\cos\omega_b$	$\mathcal{U}(-1, 1)$	$\mathcal{U}(-1, 1)$
$\sqrt{e_b}\sin\omega_b$	$\mathcal{U}(-1, 1)$	$\mathcal{U}(-1, 1)$
$q_{1;\mathrm{TESS}}$	$\mathcal{N}_{0,1}(0.296, 0.05)$	$\mathcal{N}_{0,1}(0.285, 0.005)$
$q_{2;\mathrm{TESS}}$	$\mathcal{N}_{0,1}(0.295, 0.05)$	$\mathcal{N}_{0,1}(0.304, 0.005)$
$q_{1;\mathrm{i'}}$	$\mathcal{N}_{0,1}(0.400, 0.05)$	$\mathcal{N}_{0,1}(0.343, 0.005)$
$q_{2;\mathrm{i'}}$	$\mathcal{N}_{0,1}(0.288, 0.05)$	$\mathcal{N}_{0,1}(0.309, 0.005)$
$q_{1;\mathrm{g'}}$	$\mathcal{N}_{0,1}(0.763, 0.05)$	$\mathcal{N}_{0,1}(0.688, 0.005)$
$q_{2;\mathrm{g'}}$	$\mathcal{N}_{0,1}(0.333, 0.05)$	$\mathcal{N}_{0,1}(0.359, 0.005)$
$q_{1;\mathrm{r'}}$	$\mathcal{N}_{0,1}(0.667, 0.05)$	$\mathcal{N}_{0,1}(0.597, 0.005)$
$q_{2;\mathrm{r'}}$	$\mathcal{N}_{0,1}(0.361, 0.05)$	$\mathcal{N}_{0,1}(0.377, 0.005)$
$q_{1;\mathrm{z_s}}$	$\mathcal{N}_{0,1}(0.294, 0.05)$	-
$q_{2;\mathrm{z_s}}$	$\mathcal{N}_{0,1}(0.262, 0.05)$	-
$q_{1;\mathrm{I+z'}}$	–	$\mathcal{N}_{0,1}(0.266, 0.005)$
$q_{2;\mathrm{I+z'}}$	–	$\mathcal{N}_{0,1}(0.288, 0.005)$
$q_{1;\mathrm{z'}}$	–	$\mathcal{N}_{0,1}(0.128, 0.005)$
$q_{2;\mathrm{z'}}$	–	$\mathcal{N}_{0,1}(0.287, 0.005)$
$q_{1;\mathrm{spirit}}$	–	$\mathcal{N}_{0,1}(0.133, 0.005)$
$q_{2;\mathrm{spirit}}$	–	$\mathcal{N}_{0,1}(0.288, 0.005)$
$\ln\sigma_{\mathrm{all}}$	$\mathcal{U}(-30, 1)$	$\mathcal{U}(-15, 0)$

[1]*School of Physics and Astronomy, University of Birmingham, Edgbaston, Birmingham B15 2TT, UK*
[2]*Department of Astrophysics, University of Oxford, Denys Wilkinson Building, Keble Road, Oxford OX1 3RH, UK*
[3]*Magdalen College, University of Oxford, Oxford OX1 4AU, UK*
[4]*Astrobiology Research Unit, Université de Liège, 19C Allée du 6 Août, B-4000 Liège, Belgium*
[5]*Department of Earth, Atmospheric and Planetary Science, Massachusetts Institute of Technology, 77 Massachusetts Avenue, Cambridge, MA 02139, USA*
[6]*Kavli Institute for Astrophysics and Space Research, Massachusetts Institute of Technology, Cambridge, MA 02139, USA*
[7]*Instituto de Astrofisica de Canarias (IAC), Calle Vía Láctea s/n, E-38200 La Laguna, Tenerife, Spain*
[8]*Department of Astronomy & Astrophysics, UC San Diego, La Jolla, CA 92039, USA*
[9]*Center for Astrophysics | Harvard & Smithsonian, 60 Garden Street, Cambridge, MA 02138, USA*
[10]*NASA Ames Research Center, Moffett Field, CA 94035, USA*
[11]*Instituto de Astrofisica de Andalucía (IAA-CSIC), Glorieta de la Astronomía s/n, E-18008 Granada, Spain*
[12]*Department of Physics and Astronomy, Vanderbilt University, 6301 Stevenson Center Ln., Nashville, TN 37235, USA*
[13]*Department of Physics, Engineering and Astronomy, Stephen F. Austin State University, 1936 North St, Nacogdoches, TX 75962, USA*
[14]*Universidad Nacional Autónoma de México, Instituto de Astronomía, AP 70-264, Ciudad de México 04510, México*
[15]*NASA Exoplanet Science Institute, IPAC, California Institute of Technology, Pasadena, CA 91125,USA*
[16]*Department of Physics and McDonnell Center for the Space Sciences, Washington University, St. Louis, MO 63130, USA*
[17]*Center for Space and Habitability, University of Bern, Gesellschaftsstrasse 6, CH-3012 Bern, Switzerland*
[18]*Flatiron Institute Center for Computational Astrophysics, New York, NY 10010, USA*
[19]*Komaba Institute for Science, The University of Tokyo, 3-8-1 Komaba, Meguro, Tokyo 153-8902, Japan*
[20]*European Space Agency (ESA), European Space Research and Technology Centre (ESTEC), Keplerlaan 1, NL-2201 AZ Noordwijk, the Netherlands*
[21]*Space Sciences, Technologies & Astrophysics Research (STAR) Institute, University of Liège, 19C Allée du 6 Août, B-4000 Liège, Belgium*
[22]*Institute for Particle Physics and Astrophysics, ETH Zürich, Wolfgang-Pauli-Strasse 2, CH-8093 Zürich, Switzerland*
[23]*Department of Physics and Astronomy, The University of North Carolina at Chapel Hill, Chapel Hill, NC 27599-3255, USA*
[24]*Cavendish Laboratory, JJ Thomson Avenue, Cambridge CB3 0HE, UK*
[25]*Astrobiology Center, 2-21-1 Osawa, Mitaka, Tokyo 181-8588, Japan*

This paper has been typeset from a TEX/LATEX file prepared by the author.